

Research article

## Steel slag catalyzed municipal sludge pyrolysis to produce low-pollution gas, biochar, and bio-oil products



Xiaoxuan Yang<sup>a</sup>, Guiying Xu<sup>a,\*</sup>, Huan Liang<sup>a</sup>, Hao Zhu<sup>a</sup>, Yiyu Liu<sup>a</sup>, Baizeng Fang<sup>b</sup>

<sup>a</sup> College of Chemistry and Chemical Engineering, Chongqing University of Technology, Chongqing, 400054, China

<sup>b</sup> School of Chemical Engineering and Energy Technology, Dongguan University of Technology, Dongguan, 523808, China

ARTICLE INFO

Keywords:

Steel slag  
Kinetics  
Mechanism model  
Nitrogen  
Bio-oil

ABSTRACT

This study examined the influence of steel slag powder as an additive on the pyrolysis characteristics of sludge, including the activation energy of the reactions, in addition to inhibiting the escape of nitrogen-containing and sulfur-containing gases, while improving the bio-oil fraction. There were three methods used to calculate the average activation energy of sludge: Flynn-Wall-Ozawa, Kissinger-Akahira-Sunose, and Friedman. It can be concluded that the addition of steel slag powder accelerated sludge pyrolysis and that the kinetic modeling during the primary pyrolysis stages occurred through a reaction-level mechanism model (Fn). The addition of steel slag accelerated the conversion of the elements N, C, H, and S while inhibiting the production of nitrogen- and sulfur-containing toxic gases. Adding steel slag powder reduced the amount of nitrogen-containing compounds and carboxylic acids in the bio-oil by 79.09 % and 46.40 %, respectively, while also making the oil stronger and easier to process further. This steel slag powder and sludge synergistic pyrolysis system offers numerous advantages, including energy recovery, diminished environmental consequences, and optimized resource utilization.

### 1. Introduction

With the rapid growth in global energy demand and concerns about climate change (Liu et al., 2025a), the sustainable management of ever-increasing amounts of municipal solid waste has become an important social and environmental issue (Das et al., 2019). In recent years, various solid waste management policies have been implemented around the world, with landfilling (Yang et al., 2025) and incineration (Liu et al., 2025b) being the main methods used in many countries. These methods not only face land occupation, bring serious environmental pollution, and lead to the release of greenhouse gases and harmful gases, but also increase energy consumption (Filho et al., 2024). Therefore, the adoption of solid waste disposal methods that are energy-efficient, minimizing, resourcing, and harmless is essential for the protection of the ecological environment and public health.

As a significant by-product of wastewater treatment, sewage sludge presents an urgent environmental challenge in relation to its disposal. China produced 7.8 million tons of dry sludge (Wang et al., 2025a), and the EU produced 13 million tons (Kolosionis et al., 2021) in 2019. Sludge contains a range of toxic substances, from heavy metals (Tan et al.,

2017) to pathogenic microorganisms (Wei et al., 2020) and organic pollutants (Yu et al., 2025). When disposed of improperly, sludge can elicit adverse environmental impacts, with pathogenic microorganisms and organic pollutants potentially threatening soil, plants, animals, and human health (Zheng et al., 2025). Organic matter and nutrients in sewage can improve resource recovery and sustainable development if recovered (Wu et al., 2025). Therefore, safe and effective sludge treatment has become a hot research topic and an urgent problem in the environmental field.

Sludge pyrolysis technology takes advantage of the fact that organic matter in sludge breaks down when heated without oxygen, leading to the breakdown of the organic material (Gievers et al., 2025). During the pyrolysis process, pathogens and harmful substances in sludge will be decomposed and destroyed by high temperature, and heavy metals will be immobilized in the solid products (Zhang et al., 2025b). In addition, the pyrolysis process's inert environment prevents dioxins from being released during sludge combustion and disposal (Rathnayake et al., 2025). Meanwhile, the conversion of sludge pyrolysis into products like biochar, bio-oils, and gases enables effective resource recycling (Jiang et al., 2025). Biochar has multiple applications as a soil conditioner,

\* Corresponding author.

E-mail address: [xgy092500@126.com](mailto:xgy092500@126.com) (G. Xu).

adsorbent, and catalyst (Saffari et al., 2025), and so on. Energy recovery and biofuel production are both possible with pyrolysis gas. Bio-oil can be extracted from phenols, aromatics, and other chemical raw materials, and can also be used to prepare biodiesel (Mosko et al., 2020). Recently, pyrolysis stands out from various sludge treatment technologies (Chang et al., 2025; Lv et al., 2025) and has become a popular research direction.

Steel slag is a type of solid waste produced during steel manufacturing (Lu et al., 2025). Due to its availability and low cost (Lee et al., 2020), it is advantageous for glass ceramics and construction materials (Song et al., 2019). Currently, the use rate of steel slag is only about 30 % in China (Zhu et al., 2025), with significant amounts of steel slag being wasted, which both wastes valuable land resources and produces a potential environmental hazard (Qureshi et al., 2025). Steel slag powder contains many metal oxides, such as FeO, CaO, Al<sub>2</sub>O<sub>3</sub>, and MgO, that render it catalytically active (Yu et al., 2024b). Recently, pyrolysis has emerged as a significant study domain, presenting numerous prospects for the high-value exploitation of steel slag resources. For example, Li et al. found that the presence of steel slag in heavy oil residue would help to decrease the activation energy needed for the pyrolysis of the heavy oil residue (Xiang et al., 2022). To date, little attention has been paid to sludge pyrolysis catalysis studies using steel slag, and published studies focus on kinetics studies instead of the law of nitrogen/sulfur migration and pyrolysis oil. This study primarily showcased innovation in four key areas. Initially, it utilized three "model-free" methodologies (Flynn-Wall-Ozawa, Kissinger-Akahira-Sunose, and Friedman procedures) to examine the kinetics of sludge pyrolysis accelerated by steel slag powder (SSP) and to ascertain the reaction-level mechanism model. Second, the first study on the movement of nitrogen and sulfur in this mechanism was conducted. Third, to evaluate the capacity of the alkaline component in SSP to sequester gaseous contaminants generated during sludge pyrolysis, particularly H<sub>2</sub>S. Finally, the volatile matter of SSP-catalyzed sludge pyrolysis was examined for the first time. The material mentioned fills the gaps in existing research about how sludge pyrolysis works, how nitrogen and sulfur move, the release of gas pollutants, and the volatile substances produced during pyrolysis helped by SSP. Overall, waste with waste is achieved by catalyzing sludge pyrolysis with SSP. This method not only gives SSP a way out, but it also gives sludge a low-cost and green energy utilization path.

The aims of this research report are as follows. (1) To investigate the impact of SSP as an additive on the pyrolytic properties of sludge utilizing a thermogravimetric analyzer, to assess the kinetic characteristics of sludge catalytic pyrolysis through three modeling approaches (FWO, KAS, and Friedman), and to identify the reaction mechanism model. (2) To investigate the influence of SSP on the generation profile of sludge pyrolysis gas products in an argon atmosphere by thermogravimetric infrared coupling. (3) To study how nitrogen and sulfur move during the sludge pyrolysis process using SSP, using an elemental analyzer and X-ray photoelectron spectroscopy. (4) To investigate the impact of SSP on the functional groups of sludge and pyrolysis carbon. (5) Thermal cracking gas chromatography-mass spectrometry analysis (PY-GC/MS) was employed to investigate the influence of SSP on pyrolyzed bio-oil.

## 2. Materials and methods

### 2.1. Material preparation

This dark brown, thick, and smelly sewage sludge (SS) was obtained from the Chongqing Banan District Sewage Treatment Plant. Steel slag powder (SSP) was supplied by Henan Jinrun New Material Co. The initial sludge used in the experiment had a moisture level of roughly 60 %. It was dried for about 15 h at 80 °C in a drying box until its weight remained constant. In a micro mixer, the 10 % additives and the screened 80-mesh sludge were combined for approximately half an hour. After digesting sludge samples from various mixer positions, the Ca<sup>2+</sup> content was determined using ICP-MS (PerkinElmer NexION

350D), and the homogeneity of the combined samples was confirmed based on the Ca<sup>2+</sup> concentration. Table 1 presents the elemental and industrial analysis of sludge. Table 2 presents the chemical analysis of the components of SSP disposition using XRF analysis. SSP is composed primarily of metal oxides such as CaO, Fe<sub>2</sub>O<sub>3</sub>, SiO<sub>2</sub>, MgO, Al<sub>2</sub>O<sub>3</sub>, etc. With 35.35 % of the total, CaO has the highest amount of any of them. Fe<sub>2</sub>O<sub>3</sub>, MgO, and Al<sub>2</sub>O<sub>3</sub> are presented in amounts of 27.24 %, 7.02 %, and 6.05 %, respectively.

## 2.2. Experimental methods

### 2.2.1. Thermogravimetric experiments

Tests were conducted with a thermogravimetric analyzer (NETZSCH STA 2500). The pyrolysis atmosphere for the tests was N<sub>2</sub> flowing at a constant flow rate of 50 mL/min. A weight of about 10 mg of each sample, without any added materials or chemicals, was placed into an alumina (Al<sub>2</sub>O<sub>3</sub>) crucible and heated from room temperature to 800 °C at speeds of 10, 30, and 50 °C/min, while data was automatically gathered using software. The heating rate was chosen based on a previous study (Bhushan et al., 2024; Hu et al., 2024). The selection of a 10 mg sample mainly considers sample uniformity, heat conduction efficiency, instrument detection sensitivity matching, and industry habits (Xu et al., 2022). To increase the accuracy and reliability of the experiments, the systems were calibrated prior to the experiments. The pyrolysis of the material was assessed using the pyrolysis index (CPI) as defined in Equation (1), which will be elucidated in the subsequent cited study (Chen et al., 2024).

$$\text{CPI} = \frac{(-R_p) \times (-R_a) \times M_f}{T_i \times T_p \times \Delta T_{1/2}} \quad (1)$$

Where R<sub>p</sub> and R<sub>a</sub> are the highest weight reduction percentages (%/min) and the mean reduction in weight (%/min) of the sample, respectively; M<sub>f</sub> is the mass loss of the sample (M<sub>f</sub> = m<sub>0</sub> - m<sub>∞</sub>, %); T<sub>i</sub> and T<sub>p</sub> are the initial (°C) and peak (°C) pyrolysis temperatures of the sample, respectively; and ΔT<sub>1/2</sub> is the half-peak width interval of the peak temperature of the sample (ΔT<sub>1/2</sub> = R/R<sub>p</sub> = 1/2, °C).

### 2.2.2. Tube furnace pyrolysis experiments

In the first step, approximately 3 g of the experimental sludge sample was weighed and then mixed well with a 10 % addition of SSP. The sample was then compacted to a cylindrical shape using an electronic universal testing machine (WDW-10A, Jinan Xinguang Co. Ltd.). Prior to the introduction of the sample, N<sub>2</sub> was flowing at a rate of 1 L/min and had attained the desired reaction temperature of 600 °C. N<sub>2</sub> flowed for around 30 min, and in the meantime, the tube furnace did its job of purging and cleaning the reaction chamber of air. After reaching 600 °C, the sample was placed in the center of the tube furnace for a 30-min reaction. After N<sub>2</sub> purging and the reaction took place, and then the furnace cooled to room temperature, the pyrolysis char and tar were collected for future characterization tests. A schematic representation of the experimental setup in the pyrolysis experiment using a tube furnace can be seen in Fig. 1.

Eqs. (2)–(4) provide a method for calculating the yield of pyrolysis products.

$$Y_{\text{Char}} = M_{\text{Char}} / M_0 \times 100\% \quad (2)$$

$$Y_{\text{Oil}} = M_{\text{Oil}} / M_0 \times 100\% \quad (3)$$

$$Y_{\text{Gas}} = 100\% - Y_{\text{Char}} - Y_{\text{Oil}} \quad (4)$$

Where M<sub>Oil</sub> is the weight of the recovered liquid products following drying, and M<sub>0</sub> and M<sub>Char</sub> are the weights of the sludge prior to and following pyrolysis, respectively. The yields of pyrolytic carbon, pyrolytic oil, and gas during pyrolysis are denoted as Y<sub>Char</sub>, Y<sub>Oil</sub>, and Y<sub>Gas</sub>, respectively.

**Table 1**

Ultimate analysis and Proximate analysis of SS.

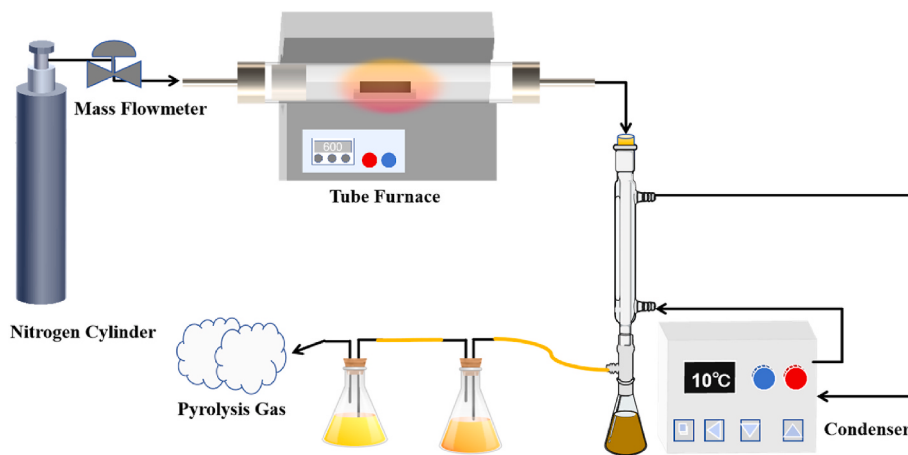
Sample	Ultimate analysis (wt%)					Proximate analysis (wt%)				LCV (kJ/kg)
	C	H	O	N	S	M <sub>ad</sub>	V <sub>ad</sub>	F <sub>Cad</sub>	A <sub>ad</sub>	
SS	10.33	1.56	45.38	2.5	1.5	7.87	54.81	19.11	18.21	560.47

Note: Mad: Moisture; Vad: Volatile Matter; FCad: Fixed Carbon; Aad: Ash; LCV: Low calorific value.

**Table 2**

The chemical composition of SSP.

Material	Oxide content (wt.%)									
	MgO	Al <sub>2</sub> O <sub>3</sub>	SiO <sub>2</sub>	P <sub>2</sub> O <sub>5</sub>	Na <sub>2</sub> O	SO <sub>3</sub>	CaO	TiO <sub>2</sub>	MnO	Fe <sub>2</sub> O <sub>3</sub>
SSP	7.02	6.05	14.37	1.06	0.9	0.69	35.35	1.26	4.57	27.24

**Fig. 1.** The experimental system for tube furnace pyrolysis schematically.

The functional group types of pyrolytic char and sludge were determined using FTIR Nicolet 8700, and the crystal structure composition of the sludge and its pyrolytic char was determined using an XRD-7000 X-ray diffraction analyzer. The XRD was performed using a Cu target with a scanning angle of 10°–80°, and a scanning speed of 3°/min. In addition, the surface distribution of elements such as N, S, and C in the sludge and pyrolytic char were examined by using a Thermo Fisher Scientific X-ray photoelectron spectroscopy (XPS K-Alpha), and all binding energies were calibrated using the standard C1s peak at 284.8 eV as a reference. The thermal cracking gas chromatography PY-GC/MS was used to analyze the chemical composition of the bio-oil.

### 2.2.3. Kinetic theory

Three approaches for isoconversion were utilized in this research: the Flynn-Wall-Ozawa (FWO), the Kissinger-Akahira-Sunose (KAS), and the Friedman (FM) methods to determine the activation energy (E<sub>a</sub>) values (Kolosisionis et al., 2021; Ling and Li, 2023). The apparent activation energy (E<sub>a</sub>, kJ/mol) was generated from the TG-DTG data using Eqs. (5)–(7).

$$\text{FWO} : \log \beta = \log \left[ \frac{AE_a}{RG(\alpha)} \right] - 2.315 - 0.4567 \frac{E_a}{RT} \quad (5)$$

$$\text{KAS} : \ln \frac{\beta}{T^2} = \ln \frac{RA}{E_a G(\alpha)} - \frac{E_a}{RT} \quad (6)$$

$$\text{FM} : \ln \frac{d\alpha}{dt} = \ln \beta \frac{d\alpha}{dT} = \ln A + \ln f(\alpha) - \frac{E_a}{RT} \quad (7)$$

Where  $\beta$  denotes the heating rate (°C/min);  $\alpha$  denotes the conversion rate (0.2–0.8);  $T$  denotes the temperature in absolute terms (K);  $R$  de-

notes the constant for universal gas (8.314 J/(mol·K)); and the function  $G(\alpha)$  denotes the integral expression of the reaction mechanism. This can be plotted by  $\log \beta$ ,  $\ln \frac{\beta}{T^2}$ , and  $\ln \frac{d\alpha}{dt}$  versus  $1/T$ , whose slope can be used to estimate E<sub>a</sub>.

### 2.2.4. Determination of kinetic modeling

Identifying the reaction mechanism model is a crucial aspect of evaluating pyrolysis kinetics. Based on the pre-calculated E<sub>a</sub> data from the FWO, KAS, and FM models, the most suitable kinetic model will be screened by the master plot method for the main pyrolysis stages (Guo et al., 2025), and the reaction mechanism will be determined for the second and third pyrolysis stages of the sludge in this study. The pyrolysis stages of this paper solely rely on the breakdown region identified in thermogravimetric analysis and do not encompass the experimental segregation of the staged pyrolysis process. The master plot method is to take the theoretical curves corresponding to a series of reaction mechanisms as a reference and compare the theoretical curves with the experimental curves so as to determine the pyrolysis reaction mechanism function (Liu et al., 2021), whose generalized formula is shown in Eq. (8).

$$G(\alpha) = \int_0^\alpha \frac{da}{f(\alpha)} = \frac{A}{\beta} \int_{T_0}^T \exp \left( -\frac{E_a}{RT} \right) dT \approx \frac{A}{\beta} \int_0^T \exp \left( -\frac{E_a}{RT} \right) dT = \frac{AE_a}{\beta R} P(u) \quad (8)$$

Where  $P(u)$  can be expressed as shown in Eq. (9), when  $u = \frac{E_a}{RT}$ , and  $P(u)$  is the temperature integral:

$$P(u) = \int_c^u -\frac{e^{-u}}{u^2} du \quad (9)$$

According to related studies (Aslan et al., 2017),  $P(u)$  can also be solved approximately by Doyle's method as shown in Eq. (10):

$$P(u) = 0.00484 \exp(-1.01516u) \quad (10)$$

where  $E_a$  and  $A$  values are calculated using  $\alpha = 0.5$  as a starting point. Adding  $\alpha = 0.5$  gives the following result (Eq. (11)):

$$G(0.5) = \frac{AE_a}{\beta R} P(u_{0.5}) \quad (11)$$

Where  $G(0.5)$  is the value of the integral reaction function at  $\alpha = 0.5$ ;  $u_{0.5} = \frac{E_a}{RT_{0.5}}$ .

Dividing Eq. (8) by Eq. (11) produces the following result (Eq. (12)):

$$\frac{G(\alpha)}{G(0.5)} = \frac{P(u)}{P(u_{0.5})} \quad (12)$$

The theoretical curve  $\frac{G(\alpha)}{G(0.5)} \sim \alpha$  is shown in the equation's left, while the experimental curve  $\frac{P(u)}{P(u_{0.5})} \sim \alpha$  is shown on the right side, and the overlap indicates the correctness of the chosen kinetic model. Table S1 shows common solid-state kinetic models.

#### 2.2.5. Fourier transform spectroscopy (FTIR) test experiments

In series, a thermogravimetric analyzer and FTIR (BRUKER TENSOR27) are employed. By using FTIR, the composition of the pyrolysis gas that was released by the thermogravimetric analyzer was examined. Use a Teflon tube to connect the TGA's outlet at 180 °C to the FTIR gas chamber, which has a 128 mm light path length, an 8.3 ml capacity, a temperature of 200 °C, and a measuring wave number between 500 and 4000 cm<sup>-1</sup>. 32 scans with a detection resolution of 4 cm<sup>-1</sup> was performed.

### 3. Results and discussion

#### 3.1. Thermogravimetric method

**Fig. 2(a) and (b)** display sludge pyrolysis TG-DTG curves of SS and SS + PSS at heating rates of 10, 30, and 50 °C/min. The results demonstrate that sludge thermal degradation has four stages: room temperature-180 °C, 180°C-400 °C, 400°C-600 °C, and 600°C-800 °C. The first stage is water evaporation (Zhao et al., 2024a), which also involves the evaporation of a small amount of bound water in the sludge. The weight loss in SS and SS + SSP ranged from 5.15 % to 7.79 % and from 7.32 % to 8.82 %, respectively, suggesting that SSP promotes water evaporation. The volatile matter decomposition phases, the second and third phases, revealed two peaks on the DTG curves. These may have been caused by the proteins, lipids, and carbohydrates in the sludge, which help break peptide bonds and open macromolecule rings (Lee et al., 2021). The DTG curve peaks at 300 °C, possibly due to small molecule organic chemical breakdown. Another peak in the DTG curve at 500°C may be due to the breakdown of hard-to-burn organic materials, high-boiling-point volatiles, and proteins (Zhao et al., 2024b). Charring and breakdown of inorganic components (e.g., CaCO<sub>3</sub>) in sludge is the fourth stage (Xiao et al., 2024).

There is evidence in Table S2 and Fig. 2(c) that as the heating rate is increased, the  $T_i$  of the two groups is shifting toward high temperature with the increase in heating rate. When compared with SS, the  $T_p$  and the half-peak width temperature range exhibit a linear relationship to heating rate with SSP. The thermal hysteresis phenomenon can occur when the peak temperature on the DTG shifts high and low T when the heating rate is increased (Guan et al., 2024). The pyrolytic process of sludge is also altered negatively because of the higher heating rate, as indicated by the slowing of the maximum weight loss rate, average weight loss rate, and CPI. The heating rate of 10 °C produces the best sludge CPI, which corresponds to the best sludge pyrolysis performance. In addition, when compared to pure sludge, the CPI at the same degree

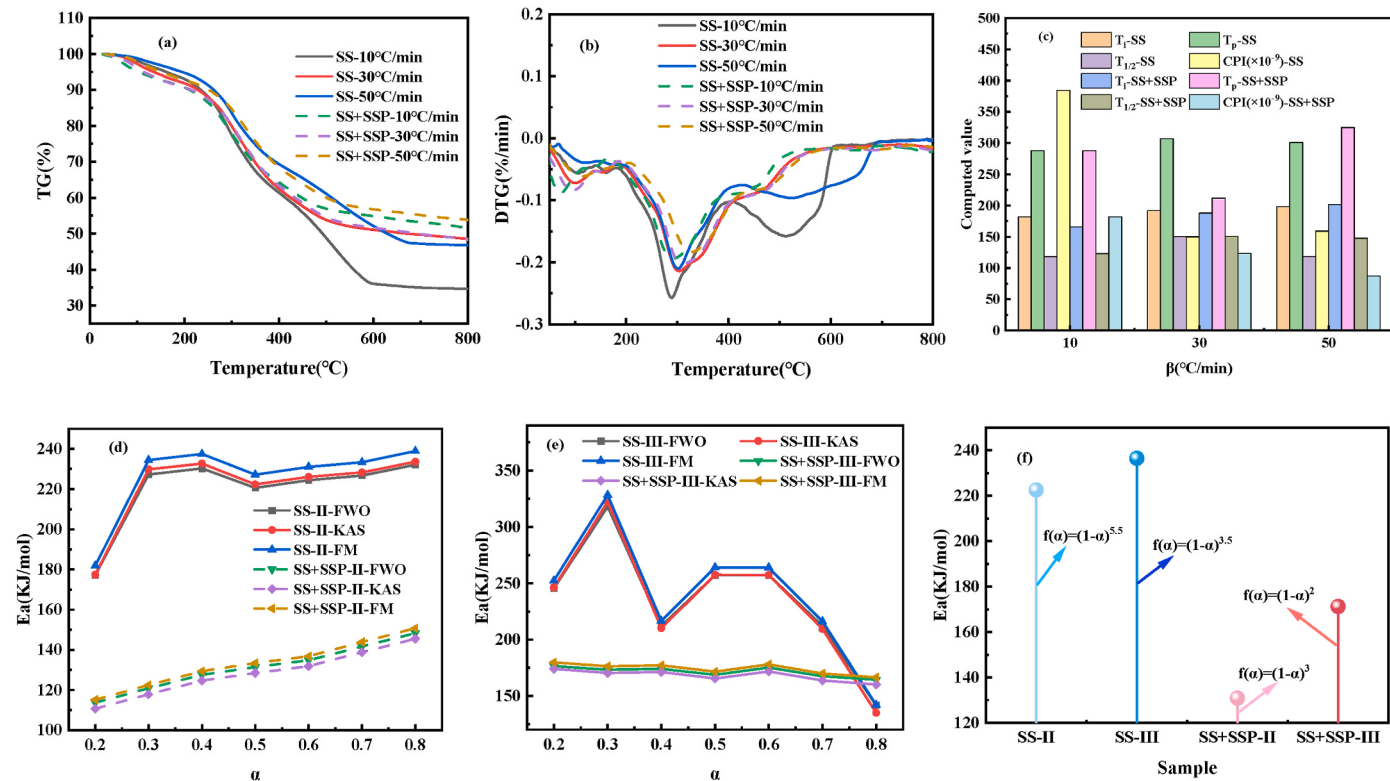


**Fig. 2.** Thermogravimetric and kinetic analysis (a) TG curves; (b) DTG curves; (c) Pyrolysis characteristic parameters; (d) The  $\alpha$  as a function of the  $E_a$  of stage II; (e) The  $\alpha$  as a function of the  $E_a$  of stage III; (f) Dynamic mechanism model.

Celsius heating rate is lower with the SSP. The decrease is attributed to influence of SSP, which is rich in the highly metal oxide (CaO, Fe<sub>2</sub>O<sub>3</sub>, MgO) and leave fewer volatile organic components in the sludge.

### 3.2. Kinetic analysis

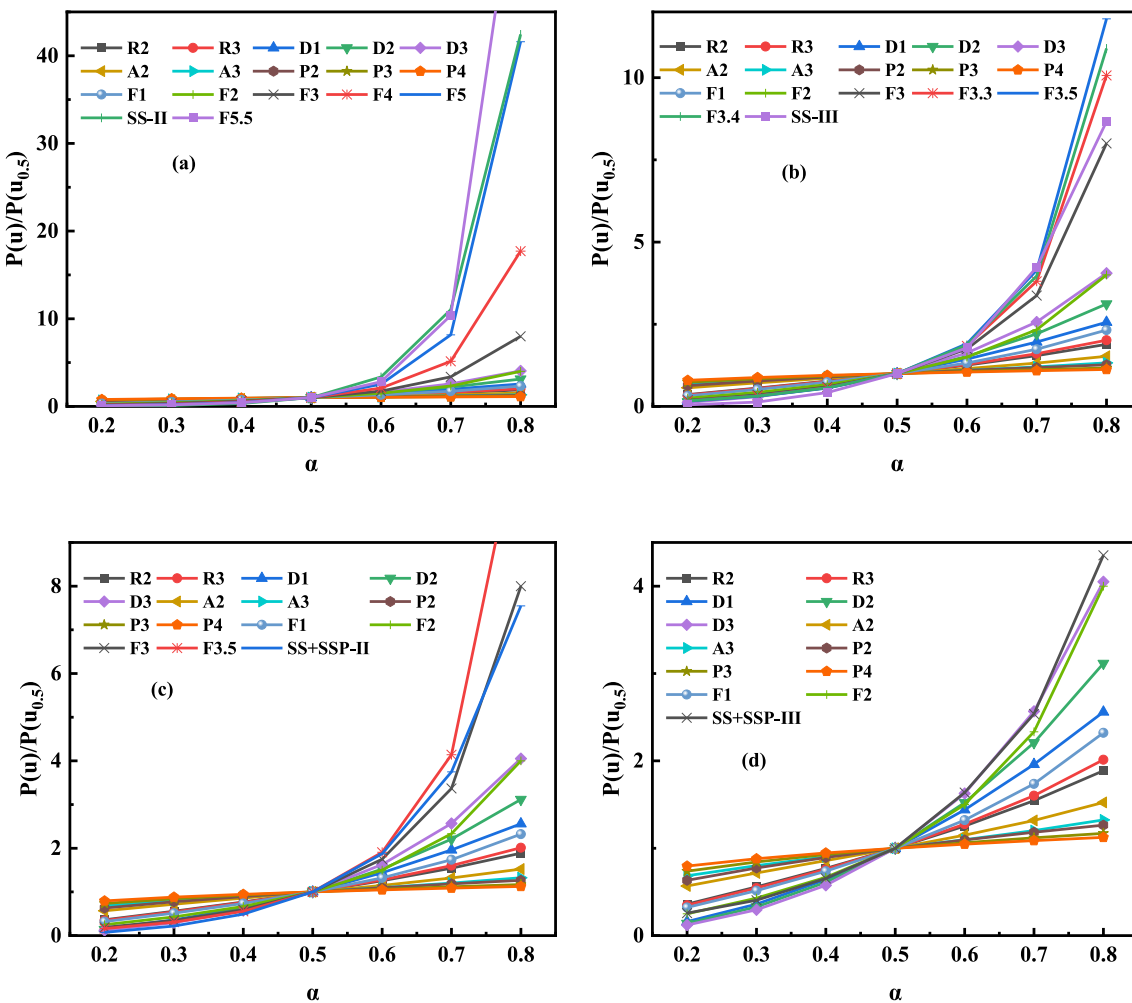
Activation energy refers to the energy needed for crossing the energy barrier required for the transition of the chemical reactants to the products within a reaction (Fu et al., 2024). High activation energy values show that the pyrolysis reaction is more challenging. The activation energies for two sets of samples based on the second and third stages are found in this study using three methods: FWO, KAS, and FM. The  $\alpha$  conversion rate in this study is applicable for between 0.2 and 0.8 in a 0.1 step size. Fitted results can be seen in Fig. S1 and S2. For each value of  $\alpha$ , the fitted determination coefficients,  $R^2$ , are greater than 0.9. To find Ea, the slopes of the fitted straight lines are used.

Fig. 2(d) and (e) show the changing pattern of Ea values with  $\alpha$  values for SS and SS + SSP pyrolysis calculated by the three methods of FWO, KAS, and FM. From Table S3, it can be seen that the average Ea values of SS pyrolysis in the second stage using the three methods of FWO, KAS, and FM are 219.85 kJ/mol, 221.48 kJ/mol, and 226.34 kJ/mol, respectively, and the average Ea values of SS pyrolysis in the third stage using the three methods of FWO, KAS, and FM are 234.89 kJ/mol, 233.99 kJ/mol, and 240.5 kJ/mol. The average Ea values for SS + SSP pyrolysis in the second stage using the three methods of FWO, KAS, and FM were 131.19 kJ/mol, 128.27 kJ/mol, and 133.12 kJ/mol, while in

the third stage, the average values of Ea were 171.35 kJ/mol, 168.12 kJ/mol, and 174.15 kJ/mol, respectively. It can be seen that the Ea values of the two groups of samples in the pyrolysis process, in the third stage, were higher than those of the second stage, which was due to the fact that the second stage mainly involves relatively weaker chemical bond rupture, which requires less energy, so the activation energy is comparatively low. The third stage primarily entails the breakdown of more stable organic matter, necessitating a higher energy input. The lower Ea value of sludge with added SSP shows that adding SSP makes it easier for the sludge to break down during pyrolysis. The lower activation energy indicates that pyrolysis requires less external energy input (Xie et al., 2023). This evidence suggests that the addition of SSP promotes sludge pyrolysis, particularly in the second stage. As SSP contains a large amount of metal oxides such as CaO and Fe<sub>2</sub>O<sub>3</sub>, it has certain catalytic activity, which makes it easier for the organic molecules in the sludge to obtain energy, resulting in the breakage and reorganization of chemical bonds, thus reducing the activation energy of the reaction.

### 3.3. Analysis of the reaction mechanism

The average values of Ea derived from the three approaches of FWO, KAS, and FM are utilized for the subsequent calculation of the response mechanism function. The Ea for the second and third stages of sludge pyrolysis of SS were 222.56 kJ/mol and 236.46 kJ/mol, respectively, while for sludge pyrolysis with added SSP, they are 130.86 kJ/mol and 171.21 kJ/mol. Fig. 3 shows the kinetic models of the pyrolysis

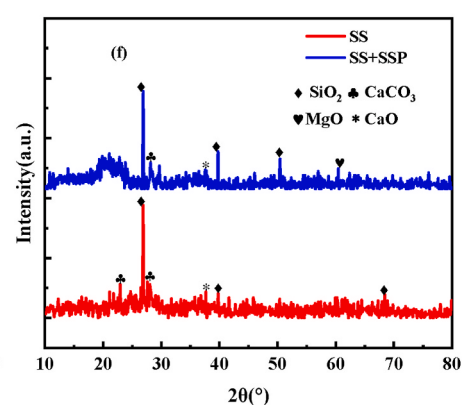
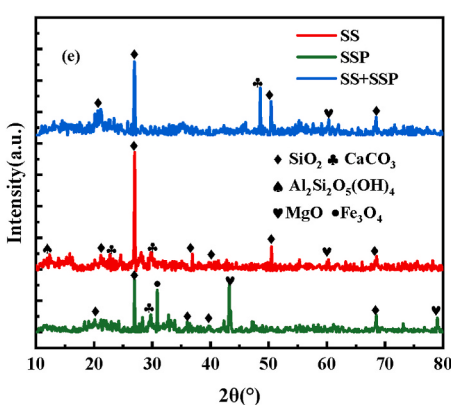
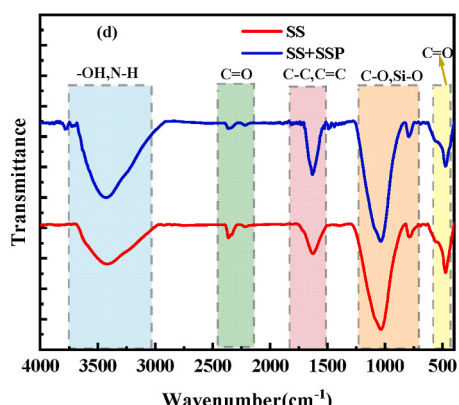
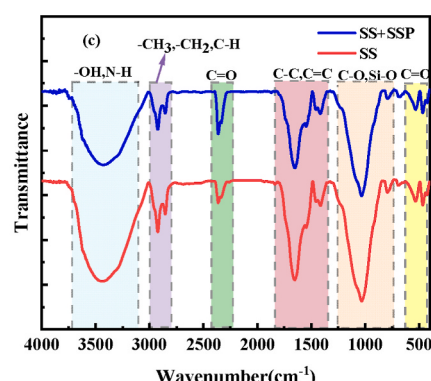
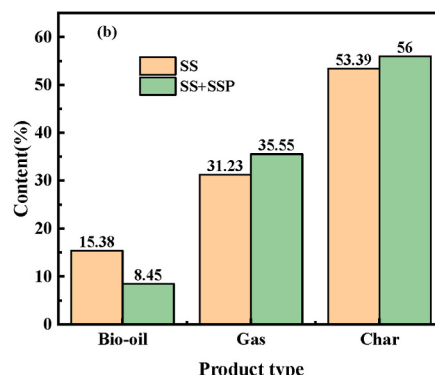
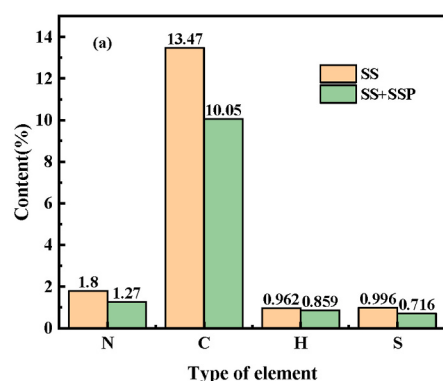


**Fig. 3.** Comparison of theoretical  $G(\alpha)/G(0.5)$  and experimental  $P(u)/P(0.5)$  values for sludge pyrolysis. (a) SS-II; (b) SS-III; (c) SS + SSP-II; (d) SS + SSP-III.

procedure that takes place in the main stages of SS and SS+SSP at 10 °C/min, and Table S4 demonstrates the corresponding kinetic models of the two stages of pyrolysis modelling. From Fig. 2(f), the experimental results for SS and SS + SSP in the second stage of pyrolysis match closely with the standard curves, which relate to the F5.5 and F3.5 reaction sequence models, respectively. The experimental curves for SS and SS + SSP fit better with the F3 and F2 reaction sequence models in the third stage of pyrolysis. These conclusions indicate that adding SSP makes the reaction process simpler, and the identified kinetic models help us better understand the reaction conditions and future designs.

### 3.4. Elemental analysis

Fig. 4(a) shows the content of four elements (N, C, H, and S) in sludge pyrolysis carbon. The results show that the content of the four elements N, C, H, and S in sludge pyrolysis char decrease after adding SSP. It indicates that SSP promoted the transformation of N, C, H, and S to other pyrolysis products, thus reducing their residual amounts in the pyrolysis char. Among them, the transformation effect of N elemental content is the most obvious. The reduction of N elemental content is 29.44 %, while the reduction of S elemental content is 28.11 %, clearly demonstrating the desulfurization effect. SSP has CaO, FeO, and other metal oxides. CaO helps break down tar (Sharifi et al., 2025) and can also react with gases that contain nitrogen and sulfur, which leads to a decrease in the amounts of N and S in the pyrolysis char. The addition of SSP reduces the C element content by 25.39 %. The addition of SSP promotes the decomposition and transformation of C. It has metals in it, like Fe and Ca, which could help break the C-C bond in organic compounds and speed up the breakdown of large molecules of organic matter into small molecules of gas. The addition of SSP reduces the content of the H element in sludge pyrolysis carbon by 10.71 %, which promotes the catalytic dehydrogenation reaction.



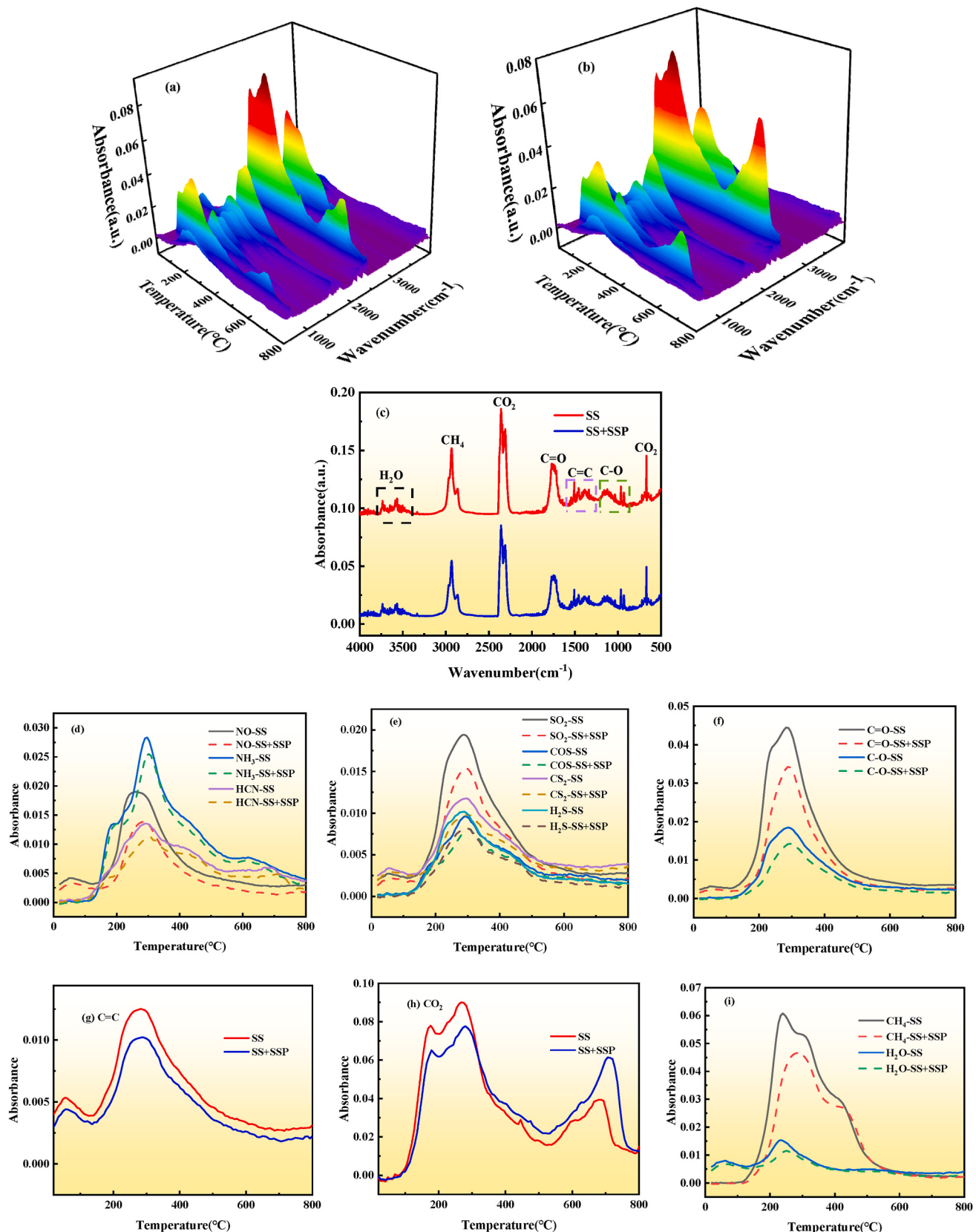
### 3.5. Three-phase product analysis

Fig. 4(b) displays how SSP affects the three-phase products of sludge pyrolysis. The findings indicate that among the three-phase products related to sludge pyrolysis, the addition of SSP results in a decrease of 45.06 % in pyrolysis oil, an increase of 13.83 % in gas, and an increase of 4.89 % in pyrolysis carbon. During pyrolysis, the metal oxides in SSP may catalyze the secondary cleavage of oil-phase precursors, and these changes may have generated even smaller molecules such as gas or more volatiles with a higher likelihood of build-up, which can explain the decline in the yield of pyrolysis oil (Hou et al., 2023). Furthermore, metal oxides may enhance the initiation of reactions such as polycondensation, cross-linking, and aromatization of oil fractions, which further reduces the yield of volatiles (e.g., pyrolysis oil) and strengthens the char structure and improves the stability of the char through a greater presence of condensed structures (Shrestha et al., 2022). Due to the higher calorific value of the gas products, they have great potential for energy recovery for both environmental and energy recovery purposes. At the same time, the greater stability of added biochar makes it more useful as a material that can soak up substances or improve soil, boosting its benefits for the environment and farming.

### 3.6. Thermogravimetric-infrared analysis

A thermogravimetric analyzer coupled with FTIR was used to study sludge pyrolysis behavior and volatile compositions (Hu et al., 2025). Pyrolysis sludge underwent depolymerization, cross-linking polymerization, dehydrogenation, and deoxygenation to create gaseous low molecular weight compounds (Lin et al., 2024). Pyrolysis gas 3D infrared absorption spectra for both sets of samples at 20 °C/min are shown in Fig. 5(a) and (b). Initial sludge weight loss is low, resulting in near-zero absorbance values for 3D-FTIR chemicals. Most pyrolysis

**Fig. 4.** Analysis of raw materials and pyrolysis products (a) Elemental analysis of sludge pyrolysis carbon and (b) Variation of three-phase products; (c) Infrared spectra of sludge; (d) Infrared spectra of pyrolyzed charcoal; (e) XRD plots of raw sample; (f) XRD plots of pyrolyzed charcoal.



**Fig. 5.** The infrared spectra of feedstock pyrolysis gas products. (a) Three-dimensional infrared spectra of SS pyrolysis; (b) Three-dimensional infrared spectra of SS + SSP pyrolysis; (c) Two-dimensional infrared spectra of feedstock pyrolysis at peak temperature; (d) Nitrogen-containing gas emissions; (e) Sulfur-containing gas emissions; (f) C=O, C-O; (g) C=C; (h) CO<sub>2</sub>; (i) CH<sub>4</sub> and H<sub>2</sub>O.

volatiles were found in the primary pyrolysis region's temperature range.

**Fig. 5(c)** illustrates absorbance occurring in the different pyrolysis stages at the peak reaction temperatures. The greatest relative intensity of gas released occurs at 268.18 °C and 280 °C for SS and SS + SSP sludge pyrolysis, respectively. According to Rombauer's Law, the concentration of gas and the absorbance have an observed positive correlation (Lin et al., 2024). Based on the evolution of the gases as shown, the order of relative intensity of gas removal can be given as follows: CO<sub>2</sub>>CH<sub>4</sub>>CO<sub>2</sub>>C=O > C=C > C-O > H<sub>2</sub>O. The H<sub>2</sub>O observed corresponds with the absorbance peaks in the wavelength region of 4000-3450 cm<sup>-1</sup>, and it is observed that at elevated temperatures the oxygen-containing functional groups decompose and react to release H<sub>2</sub>O (Huang et al., 2020). The observed absorbance peak corresponding to C-H stretching vibration at 3100-2800 cm<sup>-1</sup> allows the producer to identify CH<sub>4</sub> being released, and both sludge samples demonstrated distinct observable peaks. Two of the highest absorption peaks for CO<sub>2</sub> are located at 2400-2260 cm<sup>-1</sup> and 680–600 cm<sup>-1</sup>. The breakdown of carboxyl (-COOH), carbonyl (-C=O), and ester (-COOR) is what produces CO<sub>2</sub> (Chen et al., 2022). Similarly, it should be noted that the absorption peaks in the range of 1900-1700 cm<sup>-1</sup> correspond to C=O stretching vibration that liberated ketones, acids, and esters due to the cleavage of the epoxy functional group (Guo et al., 2024). In addition to the functional groups described above, aromatic compounds released through bending stretching vibrations of the C=C bond cause absorption maxima to occur around 1500-1300 cm<sup>-1</sup>. Two of the more common C-O stretching vibration absorbance peaks in the region of 1200-900 cm<sup>-1</sup> with hydroxyl species present suggest the production of alcohol and ether products, likely from pyrolysis. It should also be noted that with the exception of H<sub>2</sub>O, the majority of observed organic compounds were liberated between 200 °C and 600 °C.

The NH<sub>3</sub> and HCN absorption peaks are at 966 cm<sup>-1</sup> and 714 cm<sup>-1</sup>, respectively (Ahmad et al., 2025; Miskolczi and Tomasek, 2022). **Fig. 5(d)** illustrates the release intensities of NH<sub>3</sub>, HCN, and NO from sludge pyrolysis. The peak temperatures of NH<sub>3</sub> releases from SS and SS + SSP sludge are 290 °C and 301 °C, respectively. Adding SSP marginally decreases NH<sub>3</sub> release, likely because it is rich in alkaline oxides, which will affect the pyrolysis environment of sludge and make the reaction more likely to yield other products than NH<sub>3</sub>. The peak temperatures of HCN release from SS and SS + SSP sludge are around 290 °C, and pure sludge pyrolysis releases more HCN than that with SSP. NO release intensity at 1801 cm<sup>-1</sup> is SS > SS + SSP. According to **Fig. 5(d)**, SSP reduces the release of all three nitrogenous gases, although NO is most noticeable. SSP contains a lot of metal oxides, which may react with nitrogen-containing gas to fix them and reduce their release. CaO can trap acidic HCN and decrease its release. Instead of pyrolyzing huge amounts of nitrogenous compounds, SSP can convert nitrogenous organic materials, like proteins in sludge, to solid residues or more stable organic nitrogen molecules.

**Fig. 5(e)** shows that SO<sub>2</sub> and CS<sub>2</sub> have absorption peaks at 1342 cm<sup>-1</sup> and 1496 cm<sup>-1</sup>, respectively (Fang et al., 2021), while H<sub>2</sub>S and COS have absorption peaks at 992 cm<sup>-1</sup> and 867 cm<sup>-1</sup>. Decomposition and combustion of sulfur-containing substances, such as organosulfonate groups (-HSO<sub>3</sub>) and proteins, produce SO<sub>2</sub> (Ma et al., 2024). Sludge contains considerable levels of sulfate, sulfide, or sulfur-containing organics that can be transformed to H<sub>2</sub>S, CS<sub>2</sub>, and COS anaerobically, as illustrated in Eqs. (13)-(16).



SSP reduces sulfur-containing gas emission in sludge. SSP absorbs

sulfur-containing organic materials and gas in sludge due to its porous nature. As illustrated in Eqs. (17)–(21), SSP particle metal oxides like CaO and MgO interact with sulfur-containing gases to generate stable sulfides or sulfates.



**Fig. 5(h)** shows CO<sub>2</sub>'s absorption peak at 2360 cm<sup>-1</sup> (Chen et al., 2025). The linked study suggests that CO<sub>2</sub> absorption may be caused by the cleavage reformation of aliphatic and aromatic carboxyl groups, ether, quinone, and oxygen-containing heterocyclic compounds (Liu et al., 2018). As seen in **Fig. 5(f)**, the absorption peak at 1768 cm<sup>-1</sup> is ascribed to the carbonyl group's (C=O) double-bond stretching vibration, which may be connected to the cleavage of ester groups and oxidized functional groups (Zhou et al., 2022). The C-O vibration peak at 1179 cm<sup>-1</sup> may be attributed to phenolic and fatty ether molecules (**Fig. 5(f)**). **Fig. 5(g)** shows that aromatics, olefins, and other compounds have a stretching vibration C=C double bond, which may explain the 1513 cm<sup>-1</sup> absorption peak (Ma et al., 2025). As shown in **Fig. 5(h)**, SSP reduces the release of all organic compounds except CO<sub>2</sub>. SS pyrolysis releases more carbon dioxide than SS + SSP before 300 °C, and vice versa after. Carbon dioxide is made when carbohydrates and lipids decarboxylate before they break down at high temperatures, and it's also made when carbonates break down in sludge and residual carbon oxidizes after the temperatures rise. In the pre-pyrolysis stage, SSP metal ions can combine with or settle out organic matter, creating compounds that don't dissolve and reducing its production. Metal oxides in the late stage of pyrolysis oxidize remaining carbon, increasing CO<sub>2</sub> concentration. Overall CO<sub>2</sub> release intensity changes little. As illustrated in **Fig. 5(i)**, the O-H structural stretching vibration in H<sub>2</sub>O may explain the 3568 cm<sup>-1</sup> absorption peak. H<sub>2</sub>O comes from free/bound water in sludge and the cleavage or recombination of other O-H-containing functional groups. Asymmetric C-H bond stretching may explain the 2935 cm<sup>-1</sup> absorption peak. The C-H vibration generates CH<sub>4</sub>, as seen in **Fig. 5(i)**. Eqs. (22) and (23) demonstrate that C-C bonds and hydrogen radicals in aliphatic side chains form CH<sub>4</sub>.



### 3.7. Infrared analysis

**Fig. 4(c)** and (d) present a comparison of the IR spectra from raw samples and pyrolyzed carbon. Sludge IR spectra display absorption peaks in the region of 3722-3100 cm<sup>-1</sup> from the stretching vibrations of -OH on either the surface or an amide group N-H, which may broaden or sharpen the peaks we saw (Ma et al., 2023). The peak in the region of 2800–3000 cm<sup>-1</sup> is typically the stretching band of C-H, -CH<sub>3</sub>, and -CH<sub>2</sub> bonds in lipids and proteins (Osman et al., 2025). The disappearance of these peaks after pyrolysis indicates carbonization and aromatization of the sludge upon pyrolysis (Zhang et al., 2025a). The CO<sub>2</sub> peak of 2300 cm<sup>-1</sup> is likely the C=O double bond peak. The C=C double bond generated by high-temperature arylation and dehydrogenation processes contributes to the characteristic peaks in the range of 1700-1500 cm<sup>-1</sup> (Soni et al., 2024). The 1200-700 cm<sup>-1</sup> peak may be related to C-O stretching in polysaccharides and Si-O-Si vibration in silicates (Rodrigues et al., 2023), which is mainly related to quartz. The Si-O-Si is entrapped in the pyrolytic char during pyrolysis, and this conclusion is supported by XRD analysis. The permeability of C=C double bonds, C-O

bonds, and Si-O-Si bonds decreased after adding SSP, which indicates an improvement in sludge pyrolysis.

### 3.8. XRD analysis

As observed in Fig. 4(e), pure sludge, pure SSP, and sludge with SSP each display a peak for  $\text{SiO}_2$  in the X-ray diffraction plots at

approximately  $27^\circ$  and also indicate calcite ( $\text{CaCO}_3$ ) and magnesite ( $\text{MgO}$ ) mineral crystal structures. In the raw SSP material, similar features of magnetite ( $\text{Fe}_3\text{O}_4$ ) and kaolinite ( $\text{Al}_2\text{Si}_2\text{O}_5(\text{OH})_4$ ) are exhibited at the peaks of  $31^\circ$ ,  $43^\circ$ , and  $79^\circ$ , highlighting the introduction of iron oxide and aluminosilicate minerals (the kaolinite) derived by the use of SSP. In Fig. 4(f), X-ray diffraction plots are exhibited for sludge pyrolytic carbon and sludge pyrolytic carbon with SSP, with quartz remaining the

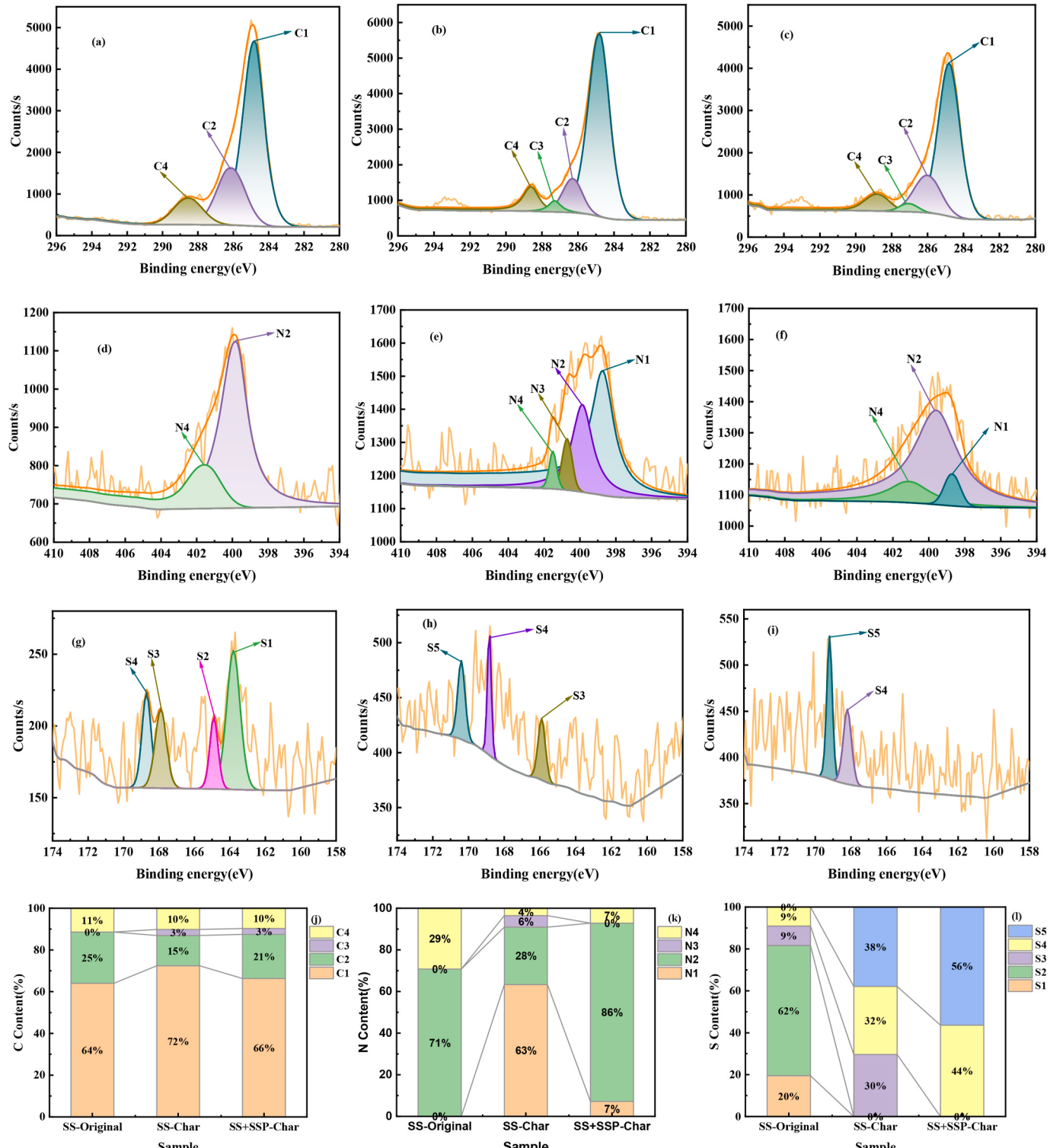


**Fig. 6.** XPS of C, N, and S (a) C1s split-peak fitting plots for sludge; (b) SS carbon of C1s; (c) SS + SSP carbon of C1s; (d) Fitted plots of N1s fractions of sludge; (e) SS carbon of N1s; (f) SS + SSP carbon of N1s; (g) S2p split-peak fits of sludge; (h) SS carbon of S2p; (i) SS + SSP carbon of S2p; (j) C; (k) N and (l) S concentrations.

primary component of the pyrolytic carbon, suggesting that thermal stability is preserved, resulting in maintaining a reconstituted structure through temperature changes (Silva et al., 2025). In both sets of samples, evidence for the crystal structure of CaO is observed, such as a peak at approximately 37.6°. This change may have occurred fortuitously when the sludge is introduced to heat and calcite decomposed. The sludge pyrolytic carbon with added SSP shows the presence of the MgO crystal structure at a peak height of 60.4°, but the sludge pyrolytic carbon without added SSP do not have MgO. Lastly, it is important to mention that the production of acidic gas or mineral components that may result from the pyrolysis process of sludge could damage the magnesium crystal structure. The take-home message for the significant data that was collected is to evaluate the potential for considering understanding mechanistic principles of mineral transformations of sludge and SSP through pyrolysis to validate and develop ideas for theoretical re-introduction for future applications.

### 3.9. XPS analysis

XPS technology can show what elements are on the surface of a material and how much of each element there is, and it can also help

analyze the functional groups on that surface in a general way and with some detail (Hua et al., 2023). XPS is used to examine the functional groups of raw sludge, sludge pyrolysis carbon, and SS+SSP pyrolysis carbon to better understand the mechanism. In this XPS study, C1s (248.8 eV) was used as a reference point to correct for charge, and Table S5 displays the detailed peak analysis for C, S, N, Fe, Ca, and Mg. The specific changes of C, N, S, Fe, Ca, and Mg compounds on the surfaces of the three groups of samples are shown in Fig. 6(a)–(i) and Fig. 7. Their deconvolution peaks and relative surface areas are shown in Table S6.

#### 3.9.1. XPS spectra of C1s

Fig. S3 presents the omnidirectional scanning broad spectra for the three sample groups. The results indicate that element O has the largest content, followed by element C. Other elements that are presented include N, S, Mg, Ca, Al, Si, and P. The C1s split-peak fitting diagrams for the three sample groups are shown in Fig. 6(a)–(c) based on the related study (Guo et al., 2023; Meng et al., 2023). The XPS spectra are separated and fitted into four peaks of 284.8 eV, 286.3 eV, 287.3 eV, and 288.6 eV, which correspond to the C-C, C-O-C, C=O, and O-C=O bonds, respectively. According to the examination, the pyrolysis charcoal has a

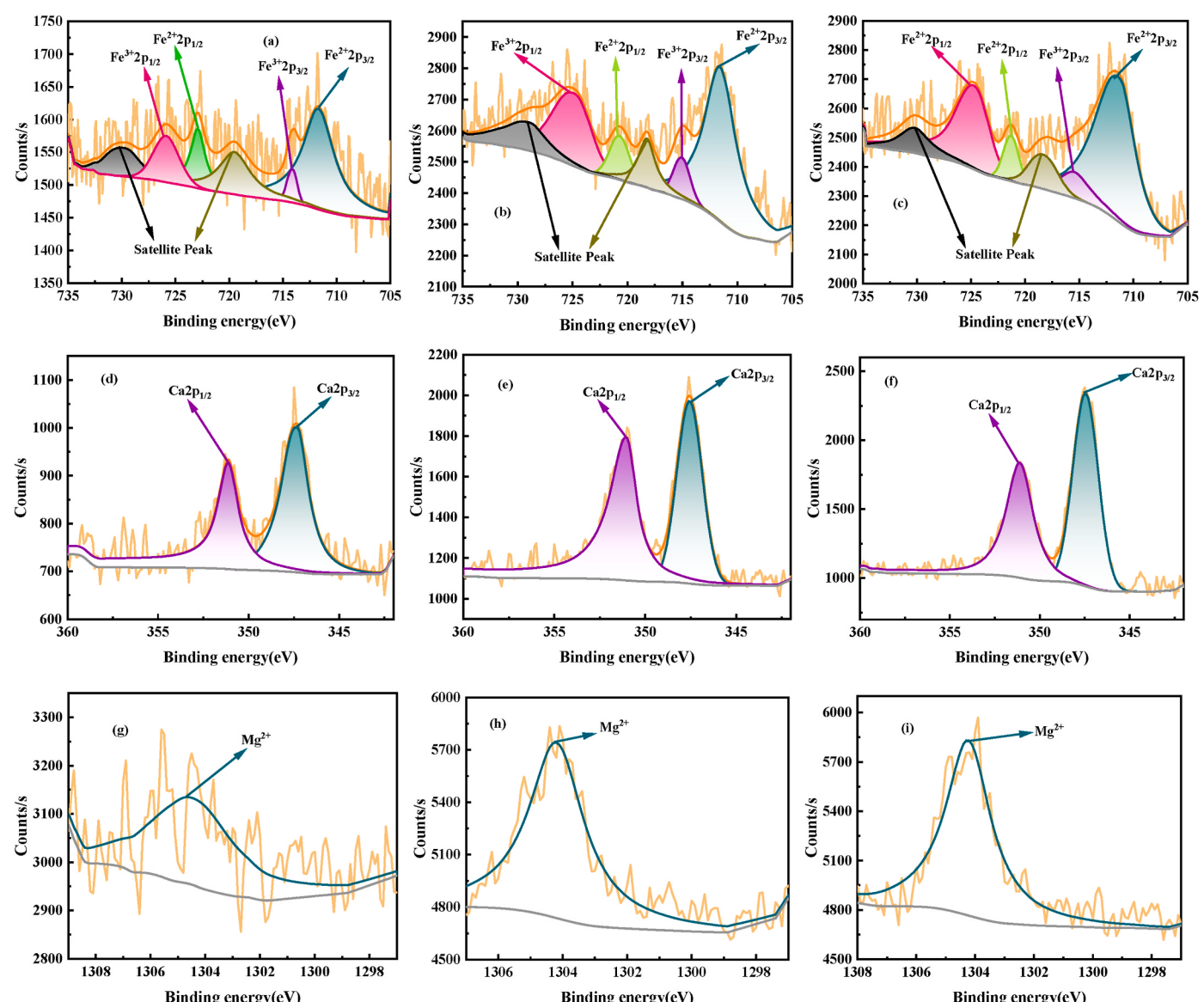
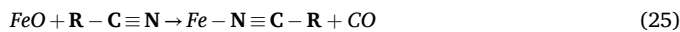


Fig. 7. Split-peak fitting of Fe2p, Ca2p, and Mg1s for sludge.

higher content of C1, and C-C (C1, 72.40 %–64.06 %) makes up the majority of the C element in the samples. Proteins, lipids, and a portion of aromatic structures are the primary sources of the C-C in the raw sludge. Higher pyrolysis temperatures are advantageous for the breakdown of aliphatic carbon chains and the creation of aromatic carbon structures, which raises the proportion of C1. Furthermore, all three samples include O-C=O (C4, 11.41 %–9.72 %) and C-O-C (C2, 24.53 %–14.51 %). The decarboxylation and dehydration reactions of some oxygen-containing functional groups, the catalytic action of metal elements in the sludge during the pyrolysis, and the fracture of organic matter in the sludge due to high temperature are all cited as the reasons for the decrease of C2 in pyrolysis char following sludge pyrolysis. Because SSP contains certain unique trace elements, such as manganese and chromium, among others, its C2 concentration is higher than that of sludge pyrolysis carbon, and its C4 content is lower than that of sludge pyrolysis carbon. It's possible that these trace elements play a unique role as catalysts in the pyrolysis process of the sludge, which breaks down C4 and creates the structure of the sludge's carbon and oxygen elements, such as C-O-C. The pyrolyzed charcoal also includes a trace quantity of C=O (C3, 2.92 %–2.83 %), which can have been caused by the sludge's decarboxylation and dehydration reactions during the pyrolysis process (Li et al., 2023).

### 3.9.2. XPS spectra of N1s

Fig. 6(d)–(f) illustrate that all fitted spectra of the N1s of sludge can be deconvoluted into four subpeaks (Du et al., 2023): amine/pyridine-N, protein-N, pyrrole-N, and inorganic/quaternary ammonium salt-N with binding energies of 398.7, 399.8, 400.5, and 401.2 eV, respectively. Fig. 6(d) illustrates that the raw sludge contained protein-N (N2, 70.75 %) and inorganic/quaternary-N (N4, 29.25 %) components. From Fig. 6(e), it can be seen that the sludge-pyrolyzed carbon mainly contained amine/pyridine-N (N1, 63.38 %) and protein-N (N2, 27.56 %), alongside trace amounts of pyrrole-N (N3, 5.54 %) and inorganic/quaternary ammonium salt-N (N4, 3.53 %) components, which implies that the proteins in the sludge were decomposed through pyrolysis and produced amines or nitrogenous substances that contain pyridine (Wang et al., 2025b). Moreover, N3 may be attributed to the cyclization of amino acids from proteins at high temperatures. Based on Fig. 6(f), it can be inferred that the sludge pyrolysis char, after being doped with SSP, was mostly composed of protein-N (N2, 78.08 %), with trace amounts of amine/pyridinium-N (N1, 6.55 %) and inorganic/quaternary ammonium salt-N (N4, 6.55 %). On the other hand, N3 is not found, suggesting that the metal oxides in SSP might help break down pyrrole-N, which comes from proteins breaking down at high temperatures (Niu et al., 2024). The nitrogen content (N4) of SSP sludge pyrolytic char is greater than that of sludge pyrolytic char due to the conversion of nitrogen into stabilized Ca<sub>x</sub>N<sub>y</sub> and Fe-N complexes at high temperatures, which transition nitrogen away from gaseous and tar contaminants and produce a rich nitrogen product. Complicated formation is illustrated through Eqs. (24)–(26).



### 3.9.3. XPS spectra of S2p

Fig. 6(g)–(i) shows that the main types of elemental sulfur in sludge are aliphatic-S, aromatic-S, sulfoxide, sulfone/sulfonic acid, and sulfate (Wang et al., 2024), with energy levels of 163.2, 164.3, 165.9, 168.8, and 170.4 eV. Virgin sludge (Fig. 6(g)) contained aliphatic-S (S1, 44.30 %), aromatic-S (S2, 14.10 %), sulfoxide (S3, 21.02 %), and sulfone/sulfonic acid (S4, 20.58 %). Aliphatic-S mainly came from sulfur-containing amino acids and sulfur ether compounds in the sludge, while aromatic-S likely originated from humus or sulfur-containing PAH

substances found in fossil fuel waste (Cheng et al., 2023). Fig. 6(h) shows peaks of elemental sulfur in the char from sludge pyrolysis, including sulfoxide (S3, 29.63 %), sulfone/sulfonic acid (S4, 32.47 %), and sulfate (S5, 37.91 %). At high temperatures, aliphatic-S and aromatic-S break down and turn into sulfur gases like H<sub>2</sub>S and SO<sub>2</sub> (Xing et al., 2024), while some are changed into sulfoxide (S3) and sulfone/sulfonic acid (S4). After adding SSP, Fig. 6(i) shows the types of elemental sulfur peaks in the sludge pyrolysis char for sulfone/sulfonic acid (S4, 43.63 %) and sulfate (S5, 56.37 %). When SSP is added, elemental sulfur can be immobilized as sulfate, and hazardous sulfur-containing gases, including SO<sub>2</sub>, can be reduced during pyrolysis. This result is consistent with thermogravimetric infrared data. Furthermore, sulfate can improve pyrolysis char's capacity to improve soil. Fig. 6(j)–(l) show the elemental content of C, N, and S.

### 3.9.4. XPS analysis of metal fractions in sludge

Fig. 7 presents the X-ray photoelectron spectroscopy (XPS) peak-fitting plots for Fe, Ca, and Mg, the three metal elements in the sludge. From Fig. 7(a)–(c), based on the derived data, Fe has six clearly distinguishable peaks at 711.5 eV, 715.4 eV, 720.7 eV, 724.8 eV, 718.3 eV, and 729.8 eV. The corresponding peak assignments include the two satellite peaks as well as the Fe<sup>2+</sup>2p<sub>3/2</sub>, Fe<sup>3+</sup>2p<sub>3/2</sub>, Fe<sup>2+</sup>2p<sub>1/2</sub> and Fe<sup>3+</sup>2p<sub>1/2</sub> tracks. From Fig. 7(d)–(f), based on its two clear peaks at 347.5 eV and 351.1 eV, which correspond to the Ca2p<sub>3/2</sub> and Ca2p<sub>1/2</sub> orbitals, the element Ca is thought to have a CaO component on the surface of the samples. Fig. 7(g)–(i) present the XPS peak-fitting plots for Mg. A distinctive peak at 1304.2 eV for the element magnesium indicates that MgO resides near the sample surface. Table S6 shows the slight increase in the Fe<sup>2+</sup>2p<sub>3/2</sub>, Fe<sup>3+</sup>2p<sub>1/2</sub> and Ca2p surface orbits in the pyrolysis char of sludge following the addition of the iron and Ca (cupola or EAF)-based SSP. This increase in the Fe and Ca surface quantities will vary with concentrations of the same elements generally present in the SSP. In addition, the iron and calcium compounds in the SSP are subjected to redox reactions with certain carbonaceous components of the sludge, such as gas, bio-oil, and pyrolytic carbon. For example, carbon can convert some of the Fe<sup>3+</sup> to Fe<sup>2+</sup>, which increases the Fe<sup>2+</sup> concentrations of pyrolytic carbon and simultaneously decreases the Fe<sup>3+</sup> content of the gas phase and the contents of the associated tracks.

### 3.10. PY-GC/MS analysis

The SS and SSP + SS sludge pyrolysis oils are complicated mixtures of many organic compounds. The pyrolysis products were identified using PY-GC/MS, and the area normalization method was used to evaluate the results of the experiment. Based on the results of PY-GC/MS analysis, products that had an 80 % or greater match were screened for analysis and discrimination purposes. Fig. 8(a) is an ion spectrogram of the volatile matter. The range indicates that over fifty total components are detected in both sampling groups, and the peak area percentage represents the relative content of different components (Table 3 and S7). Organic compounds in sludge pyrolysis oil can mainly be divided into four groups: aliphatic hydrocarbons, aromatic hydrocarbons, nitrogenous compounds, and oxygenated compounds. The oxygenated compounds include substances like aldehydes, ketones, acids, esters, alcohols, phenols, ethers, and many others (Wei et al., 2025; Yu et al., 2024a), with the main components in the pyrolysis oil shown in Fig. S4.

Table 3 shows the classification and relative content of nitrogenous compounds in the pyrolysis oils of both samples. Amine-N and nitrile-N appeared as nitrogen-containing compounds in both pyrolysis oils, while sludge pyrolysis oil contained nitrogen heterocyclic compounds. In sludge pyrolysis oil with the addition of SSP, the content of nitrogen-containing compounds decrease considerably by 79.09 %, and the stability of the tar increase. In the sludge pyrolysis process, amine-N, nitrile-N, and nitrogen heterocyclic compounds mainly originate from protein decomposition and condensation reactions.

After adding SSP, metal oxides like CaO and Fe<sub>2</sub>O<sub>3</sub> can help break

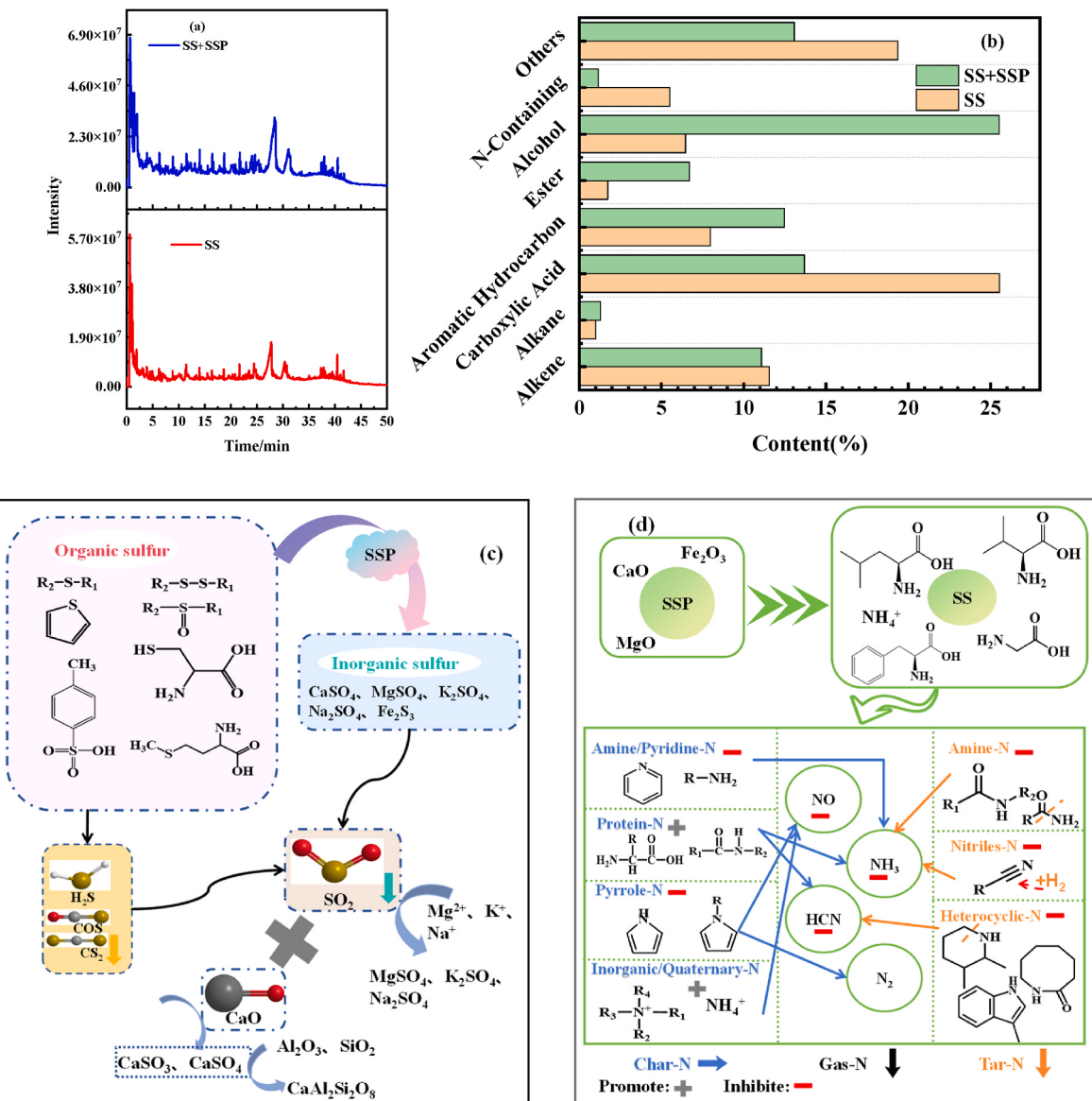


**Fig. 8.** Distribution of products to sludge pyrolysis oil and N-S conversion pathway. (a) Ion spectra; (b) Classification of products in pyrolysis oil; (c) Sulfur conversion pathway; (d) Effect of SSP on nitrogen conversion pathway.

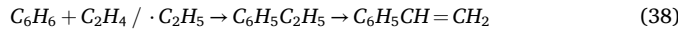
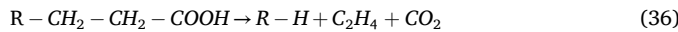
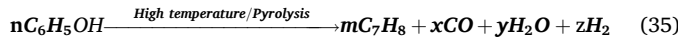
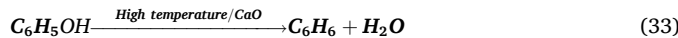
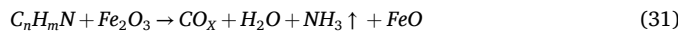
**Table 3**  
Types and contents of main nitrogen compounds in sludge pyrolysis oil.

Species	Name	Chemical Formula	Relative Content(%)	
			SS	SS + SSP
Amine	Nonadecanamide	C <sub>19</sub> H <sub>39</sub> NO	0.84	0.13
	9-Octadecenamide, (Z)-	C <sub>18</sub> H <sub>35</sub> NO	0.71	0.1
	Tetradecanamide	C <sub>14</sub> H <sub>29</sub> NO	–	0.18
SUM			1.55	0.41
Nitriles	Propanenitrile, 3-(octylamino)-	C <sub>11</sub> H <sub>22</sub> N <sub>2</sub>	0.09	–
	Benzyl nitrile	C <sub>8</sub> H <sub>7</sub> N	0.51	–
	Pentane nitrile	C <sub>5</sub> H <sub>9</sub> N	1.86	–
	Hexadecane nitrile	C <sub>16</sub> H <sub>31</sub> N	–	0.74
SUM			2.46	0.74
Heterocyclic nitrogen	Piperidine, 2,3-dimethyl-	C <sub>7</sub> H <sub>15</sub> N	0.62	–
	2-Azacyclooctanone	C <sub>7</sub> H <sub>13</sub> NO	0.5	–
	Indole, 3-methyl-	C <sub>9</sub> H <sub>9</sub> N	0.37	–
SUM			1.49	0

down amine-N and nitrile-N and also cause the structure of nitrogen-containing rings to break apart, leading to effective removal of nitrogen. The lower amount of N-containing compounds in the SS + SSP pyrolysis bio-oil makes it good for lowering NOx emissions when used as a fuel. Eqs. (27) and (28) describe how N-containing substances are formed, while Eqs. (29)–(31) might explain why there are fewer N-containing substances in the tar after adding SSP.

The formation of olefin compounds in pyrolysis oil is primarily caused by the cleavage of the alkyl side chain that is attached to the aromatic ring as well as the volatilization of small molecule compounds (Zhou et al., 2017). From Fig. 8(b) and Table S7, the olefin content of SS and SS+SSP was 11.56 % and 11.08 %, respectively, suggesting the SSP may catalyze the hydrogenation of olefin to produce saturated alkane that contribute to reducing the olefin content in the oil, which is consistent with the observation of a slight increase in the alkanes content in the pyrolysis oil. After adding SSP, the amount of carboxylic acid compounds in the tar dropped from 25.54 % to 13.69 %, a total decrease of 46.40 %, showing that SSP might stop the conversion of carboxylic acid precursors in the sludge and lower the production of carboxylic acid, which also makes the tar more stable. In the process of sludge

pyrolysis, the aromatic hydrocarbon compound content was 7.97 %, which is mainly derived from free radical cyclization of hydrocarbons or condensed aromatization of the oxygenated compounds (Reizer et al., 2022). In addition, adding SSP leads to a significant increase in aromatic hydrocarbon content to 12.47 %, an increase of 56.46 %. CaO present in SSP increases the carbon content of aromatic hydrocarbons by adsorbing the acidic intermediates from the pyrolysis of sludge and promoting the decarboxylation reaction of those by-products to aromatize them to aromatic hydrocarbon compounds. The aromatic hydrocarbons are composed mostly of toluene (5.89 %–8.39 %) simulations with styrene (1.59 %–4.08 %); the content increased along with SSP addition. Toluene in bio-oil, based on the results, is likely formed by frustrating the linkage of phenolic intermediates, and styrene is probably generated from the combination of lipids and proteins toward organic by-products and dehydrogenation of associated benzene (Li et al., 2024). Aromatic hydrocarbons are important chemical raw materials; while the enhancement of aromatic hydrocarbon content is considered to enhance the potential for further high-value utilization of the pyrolysis oil, aromatic hydrocarbon synthesis can be seen in Eqs. (32)–(38). The introduction of SSP, which acted as the framework for complete biomass decomposition, would act as a catalyst for the increased carbon content of the alcohols and ester-based oxygenates. The catalytic effect of SSP would serve to further convert the small molecules resulting from the decomposition of the macromolecules toward ester and alcohol organic compounds by catalyzing aspects of the inorganic framework toward decomposing acidic intermediates from the sludge pyrolysis. Analysis of the sludge pyrolysis bio-oil shows a composition that can be of use while providing valuable information toward the utilization of sludge pyrolysis by-products in a variety of areas; the use of SSP is effectively obtained as high-quality fuel with a combination of energy value and friendliness to the environment.



### 3.11. Mechanistic analysis of sludge pyrolysis

Fig. 8(c) illustrates the sulfur migration and transformation pattern during the sludge pyrolysis process. Following the addition of SSP, the majority of the elemental sulfur is immobilized in the pyrolysis char. When inorganic sulfide is added to SS, it encourages the sulfonation of organic sulfide and the breakdown of organic materials like thioed proteins. The process results in a rise in sulfone/sulfonic acid and

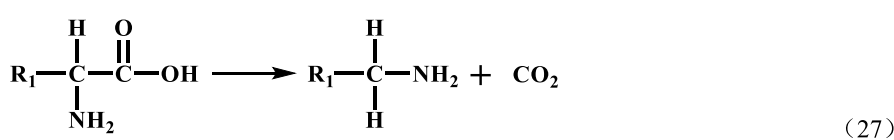
aliphatic functional groups and a fall in aromatic functional groups. While the highly stable sulfur-containing compounds break down at high temperatures to form SO<sub>2</sub>, some of the poorly stabilized sulfur-containing compounds break down during the pyrolysis of the samples to produce COS, CS<sub>2</sub>, and H<sub>2</sub>S, which are then oxidized to SO<sub>2</sub>. In the sludge, alkali metals like K, Mg, and Na react with SO<sub>2</sub> to produce the appropriate sulfates.

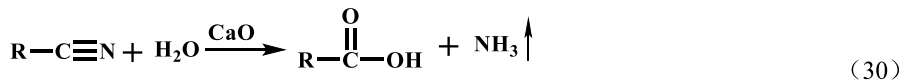
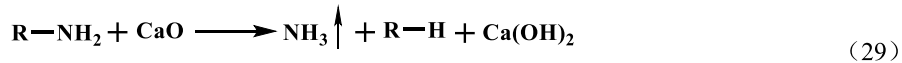
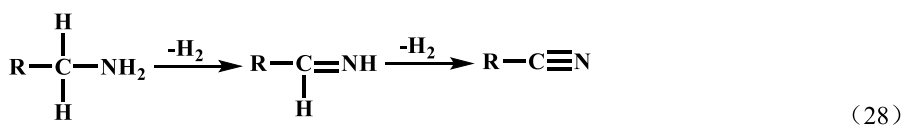
The impact of adding SSP on nitrogen conversion in sludge pyrolysis is depicted in Fig. 8(d). Nitrogen is present in coke, gas, and tar, which contained pyridine-N, pyrrole-N, protein-N, and inorganic salt-N. The gas contains NO, NH<sub>3</sub>, and HCN. And the tar contains amine nitrogen, nitrile nitrogen, and heterocyclic nitrogen substances. Ammonium salt and unstable protein decomposition were the main processes during sludge pyrolysis. After adding SSP, the metal oxides (like CaO, Fe<sub>2</sub>O<sub>3</sub>, MgO, etc.) help with the chemical reactions that break down nitrogen compounds in the tar. The intermediates, like nitrile-N and heterocyclic nitrogen, are further broken down, leading to a large amount of NH<sub>3</sub> and HCN, which are trapped by the metal oxides in the coke. In addition to preventing the production of pyridine-N and pyrrole-N, the use of SSP can also prevent the discharge of nitrogenous gas. SSP can encourage the conversion of sludge-N to inorganic salt-N and protein-N. In conclusion, SSP can immobilize the majority of the nitrogenous chemicals in coke and minimize the nitrogenous substances in sludge pyrolysis gas and tar. This capability makes it a reference for the use of sludge resources and safe disposal.

### 4. Conclusion

Pyrolysis experiments are conducted to study how SSP affects the pyrolysis of municipal sludge when added to industrial solid waste, looking at the properties of the pyrolysis products, the kinetic model, and how nitrogen and sulfur move during the process. The primary findings of the study are as follows.

- (1). The kinetic modeling during the primary pyrolysis phases follows the reaction level (Fn), and the addition of SSP lowers the activation energy in the pyrolysis process, which may encourage sludge pyrolysis.
- (2). In contrast to SS pyrolysis, the addition of SSP reduced the emission of polluting gases comprising nitrogen and sulfur while promoting the conversion of elements N, C, H, and S to other pyrolysis products.
- (3). SSP lowers the tar yield during SS pyrolysis, decreases the amount of nitrogen-containing and carboxylic acid components in the tar by 79.09 % and 46.40 %, respectively, and enhances the tar's quality.
- (4). After adding SSP, protein-N becomes the main nitrogen part in the carbon produced from sludge pyrolysis. SSP facilitates the breakdown of pyrrole-N. SSP helps improve sludge pyrolysis, enhancing the conversion of sulfur to sulfate.
- (5). Research on the pyrolysis of SSP and sludge must be thoroughly investigated due to their complex nature. To investigate the resource use of industrial solid waste and sludge, it will be important to support the optimization of the technology through multi-technology coupling in the future.





## CRediT authorship contribution statement

**Xiaoxuan Yang:** Writing – original draft, Software, Formal analysis, Data curation. **Guiying Xu:** Writing – review & editing, Resources, Project administration, Investigation, Funding acquisition, Conceptualization. **Huan Liang:** Writing – review & editing, Data curation. **Hao Zhu:** Writing – review & editing, Formal analysis. **Yiyu Liu:** Software, Data curation. **Baizeng Fang:** Project administration, Methodology.

## Funding

This work was financially supported by the National natural Science Foundation of China (21406023) and the Guangdong Provincial Natural Science Foundation Management Committee and Regional Union Fund-Regional Nurturing Project (2021B1515140055).

## Declaration of competing interest

The authors declare that they have no known competing financial interests or personal relationships that could have appeared to influence the work reported in this paper.

## Acknowledgment

This project received Grant 21406023 from the Chinese National Natural Science Foundation.

## Appendix A. Supplementary data

Supplementary data to this article can be found online at <https://doi.org/10.1016/j.jenvman.2025.126651>.

## Data availability

Data will be made available on request.

## References

- Ahmad, M.B., Embaye, T.M., Deng, S., Bukhsh, K., Ruan, R., Zhou, A., Hu, Z., Deng, N., Wu, D., Tan, H., Wang, X., 2025. Investigation on co-combustion behavior of domestic waste and sewage sludge using TG-FTIR-Py-GC/MS: thermal behavior and gaseous pollutants emission. *J. Energy Inst.* 118, 101933.
- Aslan, D.I., Parthasarathy, P., Goldfarb, J.L., Ceylan, S., 2017. Pyrolysis reaction models of waste tires: application of Master-Plots method for energy conversion via devolatilization. *Waste Manag.* 68, 405–411.
- Bhushan, D., Hooda, S., Chitransh, S., Mondal, P., 2024. Insights into catalytic co-pyrolysis of spent coffee grounds and high density polyethylene (HDPE) using acid mine drainage (AMD) treated sludge based catalyst: analysis of kinetics, mechanism and thermodynamic properties. *Sustain. Chem. Clim. Action* 5, 100051.
- Chang, Y.H., Chong, W.W.F., Liew, C.S., Wong, K.Y., Tan, H.Y., Woon, K.S., Tan, J.P., Mong, G.R., 2025. Unveiling the energy dynamics of plastic and sludge co-pyrolysis: a review and bibliometric exploration on catalysts and bioenergy generation potential. *J. Anal. Appl. Pyrolysis* 186, 106885.
- Chen, C., Qin, S., Zhu, J., He, L., Li, B., Wang, W., He, Z., 2025. Combustion characteristics, functional groups, and gaseous emission behavior of different coals by TG-FTIR. *Environ. Sci. Pollut. Res.* 32, 1–12.
- Chen, D.Y., Cen, K.H., Zhuang, X.Z., Gan, Z.Y., Zhou, J.B., Zhang, Y.M., Zhang, H., 2022. Insight into biomass pyrolysis mechanism based on cellulose, hemicellulose, and lignin: evolution of volatiles and kinetics, elucidation of reaction pathways, and characterization of gas, biochar and bio-oil. *Combust. Flame* 242, 112142.
- Chen, Z., Li, W., Huang, S., Zhuang, P., Jia, D., Evrendilek, F., Zhong, S., Ninomiya, Y., Yang, Z., He, Y., Xie, W., Liu, J., Zhuang, G., Sun, S., 2024. Dynamic, synergistic, and optimal emissions and kinetics of volatiles during co-pyrolysis of soil remediation plants with kaolin/modified kaolin. *Chem. Eng. J.* 483, 149214.
- Cheng, S., Huang, J.C., Luo, R., Tian, H., Yin, Y.S., Qiao, Y., 2023. Experimental and theoretical study on the transformation of typical organic sulfur during hydrothermal carbonization of sludge. *Fuel* 332, 126064.
- Das, S., Lee, S.H., Kumar, P., Kim, K.H., Lee, S.S., Bhattacharya, S.S., 2019. Solid waste management: scope and the challenge of sustainability. *J. Clean. Prod.* 228, 658–678.
- Du, Z.L., Zhao, P.P., Fu, Q.L., Wang, Q.D., Hu, A.B., Zhang, W.J., Wang, D.S., 2023. Biostimulants in dissolved organic matters recovered from anaerobic digestion sludge with alkali-hydrothermal treatment: nontarget identification by ultrahigh-resolution mass spectrometry. *Environ. Int.* 173, 107813.
- Fang, S.W., Lin, Y., Huang, Z., Huang, H.Y., Chen, S., Ding, L.X., 2021. Investigation of co-pyrolysis characteristics and kinetics of municipal solid waste and paper sludge through TG-FTIR and DAEM. *Thermochim. Acta* 700, 178889.
- Filho, J.F.L., Viana, R.d.S.R., Melo, L.C.A., Figueiredo, C.C.d., 2024. Changes in phosphorus due to pyrolysis and in the soil-plant system amended with sewage sludge biochar compared to conventional P fertilizers: a global meta-analysis. *Chemosphere* 371, 144055.
- Fu, J.W., Lin, S., Cai, B., Liang, J.Y., Chen, Z.B., Evrendilek, F., Zhong, S., Yang, Z.Y., Yang, C.X., He, Y., Sun, S.Y., Liu, J.Y., 2024. Catalytic co-pyrolysis of coffee grounds and polyethylene: a comparison of HZSM-5 and HY. *Fuel* 362, 130815.
- Gievers, F., Mainardis, M., Catenacci, A., Loewen, A., Nelles, M., 2025. Life cycle assessment of biochar and hydrochar derived from sewage sludge: material or energy utilization? *Cleaner Environ. Syst.* 16, 100254.
- Guan, H.Y., Wang, L., Liu, J.Y., Evrendilek, F., Chen, Z.B., Huang, S.Z., Zhong, S., Yang, Z.Y., Dai, W.C., He, Y., Yang, C.X., 2024. Energetic and environmental optimizations and byproduct valorization of pyrolysis of textile dyeing sludge with FeCl<sub>3</sub>. *J. Clean. Prod.* 434, 139940.
- Guo, K., Zhang, W.X., Gao, H.J., Yang, Y.T., Chen, J.B., 2025. Co-pyrolysis behaviors, kinetics, and thermodynamics of sludge, lignite and biomass through fixed-bed reactor experiments and thermogravimetric analysis. *Bioresour. Technol.* 417, 131871.
- Guo, N., Wang, Z., Chen, G., Zhang, M., Zhu, H., Wang, Q., Guo, S., Su, F., You, Z., Yang, S., Du, Z., Liu, Y., Lei, T., 2024. Co-pyrolysis kinetic characteristics of wheat straw and hydrogen rich plastics based on TG-FTIR and Py-GC/MS. *Energy* 312, 133683.
- Guo, W.J., Li, D.J., Zhang, Z.P., Mo, R.R., Peng, Y.Z., Li, Y.M., 2023. A novel approach for the fractionation of organic components and microbial degraders in ADM1 and model validation based on the methanogenic potential. *Water Res.* 236, 119945.
- Hou, J.H., Lin, J.H., Fang, L., Zhang, X., Ma, R., Luo, J., 2023. Microwave-catalyzed pyrolysis of waste engine oil using steel slag catalyst: structure design and insights into the intrinsic mechanism of active catalytic sites and microwave absorption functions. *Chem. Eng. J.* 471, 144171.
- Hu, B., Zhang, W.M., Guo, X.W., Li, J.H., Yang, X., Fang, Z.M., Liu, J., Lu, Q., 2025. Experimental and computational study on xylan pyrolysis: the effect of branch structures. *Fuel* 386, 134329.

- Hu, Y., Xia, Z., Wang, X., Xing, B., Chen, Q., Yu, F., Zhou, N., 2024. Enhanced co-pyrolysis of textile and leather waste with Ca/Fe-enriched sludge ash: catalytic effect on thermal behavior, volatile composition, and biochar formation. *Fuel* 373, 132272.
- Hua, L., Yu, L.M.F., Dang, F.L., Zhao, H., Wei, T., 2023. Preparation of sludge-based biochar loaded with ferromanganese and its removal mechanism of tetracycline hydrochloride. *Environ. Sci. Pollut. Res.* 30, 101099.
- Huang, H., Liu, J., Liu, H., Evrendilek, F., Buyukada, M., 2020. Pyrolysis of water hyacinth biomass parts: bioenergy, gas emissions, and by-products using TG-FTIR and Py-GC/MS analyses. *Energy Convers. Manag.* 207, 112552.
- Jiang, Z.Q., Liang, Y.N., Zhu, S., Zheng, K., Zhu, Y.J., Yang, D.H., Wang, H.L., Fu, P.B., 2025. Hydrogen production by suspension self-rotation enhanced pyrolysis of sludge particles in cyclone. *Water Res.* 275, 123198.
- Kolosionis, A., Kastanaki, E., Veksha, A., Wang, H.M., He, C., Lisak, G., Giannis, A., 2021. The effects of washing techniques on thermal combustion properties of sewage sludge chars. *Int. J. Environ. Res.* 15, 285–297.
- Lee, S., Kim, Y.M., Siddiqui, M.Z., Park, Y.K., 2021. Different pyrolysis kinetics and product distribution of municipal and livestock manure sewage sludge. *Environ. Pollut.* 285, 117197.
- Lee, T., Jung, S., Park, Y.K., Kim, T., Wang, H., Moon, D.H., Kwon, E.E., 2020. Catalytic pyrolysis of polystyrene over steel slag under CO<sub>2</sub> environment. *J. Hazard. Mater.* 395, 122576.
- Li, G., Wang, Z.H., Zuo, L.L., Zhang, T., Xiao, W.B., Yang, T.L., Tursunov, O., Zhao, N., Zhou, Y.G., 2024. Regulating phenol tar in pyrolysis of lignocellulosic biomass: product characteristics and conversion mechanisms. *Bioresour. Technol.* 409, 131259.
- Li, J.W., Jin, J., Zhao, Y.N., Zou, Z.W., Wu, Y.C., Sun, J.T., Xia, J.X., 2023. Enhancing phosphorus bioavailability in sewage sludge through co-hydrothermal treatment with biomass. *J. Water Process Eng.* 51, 103448.
- Lin, L., E, Y., Sun, Q., Chen, Y., Dai, W., Bao, Z., Niu, W., Meng, J., 2024. Analysis of the pyrolysis kinetics, reaction mechanisms, and by-products of Rice Husk and Rice straw via TG-FTIR and Py-GC/MS. *Molecules* 30, 10.
- Ling, C.C.Y., Li, S.F.Y., 2023. Synergistic interactions between sewage sludge, polypropylene, and high-density polyethylene during co-pyrolysis: an investigation based on iso-conversional model-free methods and master plot analysis. *J. Hazard. Mater.* 455, 131600.
- Li, C.L., Li, Y.X., Fan, D.K., Zhu, P.F., Liu, Y., Chao, L., Zhou, C.B., Yao, B., Zhang, Y.W., Dai, J.J., 2025b. In situ catalytic pyrolysis of oily sludge using coal gangue char to produce naphthalene-rich oil and hydrogen-rich gas. *Chem. Eng. J.* 508, 130953.
- Liu, H.D., Xu, G.R., Li, G.B., 2021. Pyrolysis characteristic and kinetic analysis of sewage sludge using model-free and master plots methods. *Process Saf. Environ. Prot.* 149, 48–55.
- Liu, L.L., Wang, Z.Q., Che, K., Qin, Y.K., 2018. Research on the release of gases during the bituminous coal combustion under low oxygen atmosphere by TG-FTIR. *J. Energy Inst.* 91, 323–330.
- Liu, Y.J., Wang, S., Lyu, Z., Zheng, Y., Gao, H., Wang, J.B., 2025a. Comprehensive analysis of bio-syngas production via the co-pyrolysis of sewage sludge and cotton stalk: products, optimal conditions, kinetics, and synergistic effects. *J. Anal. Appl. Pyrolysis* 186, 106980.
- Lu, Y., Liu, K., Yuan, Z.F., Zhao, H.X., Xu, B.S., 2025. Innovative strategies for thermal storage of steel slag-modified porous ceramic-based low-temperature composite phase change materials. *J. Energy Storage* 113, 115622.
- Lv, M.Y., Zhao, T.T., Chen, J.J., Tong, L.Z., Ni, Z.B., Lin, Q.Q., Ruan, Z.P., Qiu, R.L., 2025. Distribution and transformation behavior of heavy metals and phosphorus during sewage sludge pyrolysis. *Environ. Technol. Innov.* 37, 104049.
- Ma, W.X., Ma, Q.H., Zhao, Y.Y., Hu, X.M., He, Z.L., Chi, L.H., Zhao, X.X., Zhao, Y.X., Sun, F., Chu, C.Y., 2023. Preparation and resource utilization of sludge-based fire-preventive and extinguishing composite gel for coal mine. *J. Environ. Chem. Eng.* 11, 109465.
- Ma, X., Ning, H., Xing, X., Zang, Z., 2025. Co-pyrolysis behaviors and reaction mechanism analyses of coal slime and moso bamboo based on GC/MS and backpropagation neural network. *Int. J. Hydrogen Energy* 98, 197–210.
- Ma, X.F., Ning, H.F., Zhang, X.F., Zang, Z.J., Xing, X.J., 2024. Co-combustion characteristics of coal slime and moso bamboo based on artificial neural network modeling and TG-FTIR. *Energy* 313, 133816.
- Meng, X.Y., Song, T.T., Zhang, C., Wang, H.Y., Ge, M., Guo, C.S., 2023. Magnetic MnFe<sub>2</sub>O<sub>4</sub> nanoparticles anchored on sludge-derived biochar in activating peroxydisulfate for levofloxacin degradation: mechanism, degradation pathways and cost analysis. *J. Environ. Chem. Eng.* 11, 110241.
- Miskolci, N., Tomasek, S., 2022. Investigation of pyrolysis behavior of sewage sludge by thermogravimetric analysis coupled with Fourier transform infrared spectrometry using different heating rates. *Energies* 15, 5116.
- Mosko, J., Pohorely, M., Skoblia, S., Beno, Z., Jeremiás, M., 2020. Detailed analysis of sewage sludge pyrolysis gas: effect of pyrolysis temperature. *Energies* 13, 4087.
- Niu, Q., Du, X., Li, K., Lu, Q., Ronse, F., 2024. Role of catalyst porosity and acidity in nitrogen transformation during catalytic fast pyrolysis of microalgae: study on extracted protein and model amino acids. *Energy Convers. Manag.* 322, 119210.
- Osman, N.B., Armin, U.S.B.M., Patrick, D.O., Zaman, N.A.B.B.N., Saadon, S.Z.A.H., Yusup, S., Yahya, L., 2025. Pyrolysis and kinetic analysis of marine (*Isochrysis* sp.) and freshwater (*Monoraphidium* c.) microalgae. *Energy Convers. Manag.* X 26, 100904.
- Qureshi, H.J., Alghamdi, S.A., Majdi, A., Ahmad, J., Rahmawati, C., Alattyih, W., Alzlfawi, A., 2025. Utilization of steel slag in concrete: a review on durability and microstructure analysis. *Rev. Adv. Mater. Sci.* 64, 20250086.
- Rathnayake, N., Sivaram, A.K., Hakeem, I.G., Pabba, S., Patel, S., Gupta, R., Paz-Ferreiro, J., Sharma, A., Megharaj, M., Surapaneni, A., Shah, K.L., 2025. The fate of per- and polyfluoroalkyl substances (PFAS) during pyrolysis and co-pyrolysis of biosolids with alum sludge and wheat straw. *J. Anal. Appl. Pyrolysis* 187, 106970.
- Reizer, E., Viskolcz, B., Fiser, B., 2022. Formation and growth mechanisms of polycyclic aromatic hydrocarbons: a mini-review. *Chemosphere* 291, 132793.
- Rodrigues, J.L., Campelo, J.D., Wisniewski, A.W., Hantao, L.W., Eberlin, M.N., Santos, J. M., 2023. Chemical evaluation of pyrolysis oils from domestic and industrial effluent treatment station sludges with perspective to produce value-added products. *Waste Manag.* 168, 202–210.
- Saffari, M., Moazallahi, M., Mashayekhi, R., 2025. The fate and mobility of chromium, arsenic and zinc in municipal sewage sludge during the co-pyrolysis process with organic and inorganic chlorides. *Sci. Rep.* 15, 2986.
- Sharifi, M., Tangestaninejad, S., Moghadam, M., Marandi, A., Mirkhani, V., Baltork, I.M., Aghayani, S., 2025. Metal-organic frameworks-derived CaO/ZnO composites as stable catalysts for biodiesel production from soybean oil at room temperature. *Sci. Rep.* 15, 3610.
- Shrestha, P., Chun, D.D., Kang, K., Simson, A.E., Klinghoffer, N.B., 2022. Role of metals in biochar production and utilization in catalytic applications: a review. *Waste Biomass Valoriz.* 13, 797–822.
- Silva, L., Miranda, F., Moreira Jr., P., Ferreira, A., Fuji, M., Cruz, A., Essiptchouk, A., Petracconi, G., 2025. Investigating chemical changes, material properties, and off-gas emissions in sewage sludge through thermal plasma treatment. *J. Environ. Manag.* 375, 124256.
- Song, Q., Zhao, H.Y., Jia, J.W., Zhang, F., Wang, Z.P., Lv, W., Yang, L., Zhang, W., Zhang, Y., Shu, X.Q., 2019. Characterization of the products obtained by pyrolysis of oil sludge with steel slag in a continuous pyrolysis-magnetic separation reactor. *Fuel* 255, 115711.
- Soni, N.K., Prabhansu, Bhale, P.V., 2024. Chemical insight into thermal degradation, chemical kinetics, and thermodynamics behavior of sewage sludge through thermogravimetry and Fourier transform infrared analysis. *Therm. Sci. Eng. Prog.* 51, 102617.
- Tan, P., Ma, L., Xia, J., Fang, Q.Y., Zhang, C., Chen, G., 2017. Co-firing sludge in a pulverized coal-fired utility boiler: combustion characteristics and economic impacts. *Energy* 119, 392–399.
- Wang, C.K., Yang, X.X., Hassan, B., Yu, C., He, H., Xu, Z.X., Huang, B., Pan, X.J., 2025b. Synergistic pyrolysis mechanism of typical organic components of sewage sludge in the presence of CaO: lipids, proteins, and polysaccharides. *Fuel* 380, 133213.
- Wang, Y.L., Ye, L., Chen, Y., Li, J.K., Bai, T., Jin, Z.P., Jin, Y., 2024. Sulfur migration and conversion during co-combustion of sewage sludge and coal slime. *Renew. Energy* 237, 121646.
- Wang, Z.J., Gui, X.W., Luan, H.L., Li, Z.L., Zeng, Y.F., Zheng, Y., 2025a. Permanganate pretreatment improves the production of short chain fatty acids from waste activated sludge at pH10: performance and mechanism. *Sep. Purif. Technol.* 362, 131692.
- Wei, L., Zhu, F., Li, Q., Xue, C., Xia, X., Yu, H., Zhao, Q., Jiang, J., Bai, S., 2020. Development, current state and future trends of sludge management in China: based on exploratory data and CO<sub>2</sub>-equivalent emissions analysis. *Environ. Int.* 144, 106093.
- Wei, Y., Wu, Y., Du, Z., Zhang, X., Xu, J., Xu, K., Jiang, L., Wang, Y., Su, S., Hu, S., Xiang, J., 2025. Interaction mechanisms of coal macerals during pyrolysis: insights from TG and Py-GC/MS experiments combined with ReaxFF MD simulations. *Chem. Eng. J.* 504, 158768.
- Wu, Y., Yu, Y., Wang, Y., Pan, X.W., Shi, W.J., Huang, Y.J., Liao, Y., Yang, Y.Y., Zuo, X.Y., 2025. The effect of cyclic catalytic pyrolysis system on the co-pyrolysis products of sewage sludge and chicken manure, focusing on the yield and quality of syngas. *Energy* 314.
- Xiang, L., Li, H.W., Qu, Q.P., Lin, F.W., Yan, B.B., Chen, G.Y., 2022. In-situ catalytic pyrolysis of heavy oil residue with steel waste to upgrade product quality. *J. Anal. Appl. Pyrolysis* 167, 105676.
- Xu, G., Cai, X., Wang, S., Fang, B., Wang, H., Zhu, Y., 2022. Characteristics, kinetics, infrared analysis and process optimization of co-pyrolysis of waste tires and oily sludge. *J. Environ. Manag.* 316, 115278.
- Xiao, T., Zhou, P.K., Liu, Y., Zhang, K.K., Liu, F.Y., Guo, G., Ni, F.Q., Deng, Y., 2024. Impact of pyrolysis temperature on heavy metals environmental risk in biochar derived from co-pyrolysis of *Alternanthera philoxeroides* and sludge. *J. Environ. Chem. Eng.* 12, 114841.
- Xie, W., Su, J., Zhang, X.K., Li, T., Wang, C., Yuan, X.Z., Wang, K.G., 2023. Investigating kinetic behavior and reaction mechanism on autothermal pyrolysis of polyethylene plastic. *Energy* 269, 126817.
- Xing, Y.X., Huang, J.C., Wang, Z.Q., Hu, W., Xu, M.H., Qiao, Y., 2024. Transformation and control of organic sulfur during pyrolysis of sludge under conditions relevant to smoldering combustion: role of oxygen and CaO. *Energy* 309, 133143.
- Yang, H.Q., Li, Z.Y., Yan, L.J., Zhang, K., Wang, X.Z., Li, X.L., Wang, M.J., Wang, J.C., Chang, L.P., Bao, W.R., 2025. Study on the formation mechanism of thermal coke during sludge pyrolysis. *Fuel* 392, 134826.
- Yu, G., Bai, X., Fan, X., He, X.Y., Zou, H.X., Dilixiat, Y., Wei, X.Y., Pidamaimaiti, G., Pan, Y., 2024a. In-situ evaluation of volatile products released during pyrolysis of coals with different ranks. *J. Energy Inst.* 115, 101660.
- Yu, H., Li, Z.W., Yu, D., Huang, J.X., Zou, X.Y., Wang, Y., 2025. Removal of high concentration chlorides and organic pollutants from incineration fly ash and sewage sludge hydrothermal liquid by Friedel's salt preparation. *J. Environ. Manag.* 375, 124383.
- Yu, H.D., Lin, F.W., Guo, X., Yao, H.Y., Zheng, F., Li, J.T., Zhang, M., Li, R.D., Yan, B.B., Chen, G.Y., 2024b. Co-pyrolysis of saw dust and oily sludge with waste-heat utilization of steel slag on rotary kiln simulated engineering practice. *Fuel* 364, 131012.

- Zhang, Y., Zhao, X., Chen, S., 2025a. Catalytic effects of different metal salts on cotton waste textiles by pyrolysis: pyrolysis behavior and properties of activated carbon. *Text 5*, 4.
- Zhang, Z.H., Cheng, L., Hu, Q.X., Hu, Z.Q., 2025b. Influence of pyrolysis temperature on speciation, leaching and environmental risk assessment of heavy metals in biochar and bio-oil from pyrolysis of wet sewage sludge. *Biomass Convers. Biorefin.* 1–14.
- Zhao, H.B., Wang, X.W., Liu, J.F., Li, S.J., Yang, T.X., Xi, B.D., 2024a. Nitrogen recycling characteristics in multiphase transformation during municipal sludge pyrolysis. *J. Clean. Prod.* 457, 142475.
- Zhao, X.M., Wan, C.L., Pan, Y.T., Fan, Y., Liu, X., 2024b. Pyrolysis behavior of sewage sludge coexisted with microplastics: kinetics, mechanism, and product characteristics. *J. Environ. Manag.* 370, 123030.
- Zheng, X.Y., Hu, Y., Xiao, Z.K., Feng, Y.H., Ying, Z., Wang, B., Dou, B.L., 2025. Activation of peroxymonosulfate by iron-containing sewage sludge pyrolytic hydrochar-based catalyst for efficient treatment of process water. *J. Environ. Chem. Eng.* 13, 115341.
- Zhou, D., Chen, X.P., Liang, J.Z., Wei, X.J., Wu, C.H., He, Y.L., Wang, L.L., 2022. Combustion kinetics and fuel performance of tackifying resins by TG-FTIR and DFT analysis. *Fuel* 330, 125656.
- Zhou, P., Xiong, S., Zhang, Y., Jiang, H., Chi, Y., Li, L., 2017. Study on the nitrogen transformation during the primary pyrolysis of sewage sludge by Py-GC/MS and Py-FTIR. *Int. J. Hydrogen Energy* 42, 18181.
- Zhu, G.H., Zhang, Y.S., Zhang, Y., Wu, M., Zhang, J.F., Wang, Z.Y., Fan, D.D., Chen, J., 2025. Study on the mechanical properties of sodium hydroxide activated steel slag for loess improvement. *Mater. Lett.* 385, 138179.